Manipulation of the Plasmonic Properties of n-Type Doped Colloidal Indium Oxide Nanocrystals

by

Hanbing Fang

A thesis

presented to the University of Waterloo

in fulfillment of the

thesis requirement for the degree of

Master of Science

in

Chemistry-Nanotechnology

Waterloo, Ontario, Canada, 2017

Author's Declaration

I hereby declare that I am the sole author of this thesis. This is a true copy of the thesis, including any required final revisions, as accepted by my examiners. I understand that my thesis may be made electronically available to the public.

Abstract

Plasmonic nanocrystals (NCs) have been a focus of intense research over the past decade due to their unique optical properties and wide applications. Indium (III) oxide (In_2O_3) is an ideal host lattice for plasmonic NCs, owing to its high charge carrier concentration and mobility. In this project, one pot colloidal synthesis has been utilized to prepare antimony-doped In_2O_3 (AIO) NCs and titanium-doped In_2O_3 (TIO) NCs. It is shown that both of these doped NC samples exhibit the tunability of the plasmon resonance in the mid-infrared (MIR).

For AIO NCs, it is revealed that the plasmon resonance can be well-tuned from 0.25 eV to 0.37 eV, with the maximum electron concentration of ca. 1.24×10^{20} cm^{-3} determined for 10.6 % of Sb. Compared to the broad plasmon of AIO NCs, relatively narrow plasmon of TIO NCs can be tuned from 0.13 eV to 0.28 eV by varying the doping concentration of Ti from 1.12 % to 7.8 %. Furthermore, the highest electron concentration determined for TIO NCs (7.8 % of Ti) is ca. 6.85×10^{19} cm^{-3}.

Both XRD patterns and high-resolution TEM images indicate that all synthesized AIO and TIO NCs retain the body-centered cubic (bcc)-In_2O_3 structure. UV-visible absorption spectra confirm the blue shift of the band gap for both AIO NCs and TIO NCs, because of the Burstein-Moss effect. Post treatment of as-synthesized NCs by rapid annealing under H_2 or Ar illustrates that the intensity of the plasmon band can be improved appreciably. Finally, electronic and optical properties of AIO and TIO NCs were further investigated by the Density Functional Theory (DFT) calculations.

It is expected that broadly tunable AIO and TIO NCs in the MIR can be employed in a variety of potential applications, including sensing, enhanced spectroscopy, and thermal imaging.

Acknowledgements

Firstly, I would like to express my sincerest appreciation to my supervisor Dr. Pavle Radovanovic for all his continued guidance and support throughout the project. It is his constructive comments on research and passion for science that encouraged me to face many challenges I encountered during my M.Sc. program. Gratitude is extended to my committee members Dr. Michael Pope and Dr. Juewen Liu for their insightful comments and feedbacks on my seminar proposal and thesis.

My project would not have been accomplished without the support from many talented and helpful people. I would like to acknowledge Dr. Carmen Andrei for her assistance in TEM image collection at McMaster University. I also thank Quanquan Pang in Nazar's group for his aid in FTIR measurement at the University of Waterloo. I would like to acknowledge Yixuan Shi from the Kleinke lab, at the University of Waterloo for her help with XRD patterns collection.

I would also like to thank all my past and present group members for their helpful encouragement and suggestions. It is always my great pleasure to work closely with current team members Manu, Vahid, Paul, Natalie, Penghui, Yi, and Yunyan. Firstly, I acknowledge Vahid for helping me get off a good start of my project and watching out the safety issues in the lab all the time. In addition, I am really appreciative of Penghui's assistance in Raman spectrum measurement. Particularly, I would like to thank Manu for his simulation of my synthesized material and fruitful data discussion.

Last but not least, I am genuinely grateful to my parents and my sister for their continuous encouragement and love during my pursuit of the master.

Table of Contents

List of Figures

List of Tables

List of Abbreviations

Acac	Acetylacetonate
AIO	Antimony-doped Indium Oxide
bcc	Body-centered cubic
CB	Conduction Band
DFT	Density Functional Theory
eq	Equation
FTIR	Fourier Transform Infrared Spectroscopy
FWHM	Full Width At Half-maximum
GGA	Generalized Gradient Approximation
HRTEM	High-resolution TEM
MIR	Mid-Infrared
NCs	Nanocrystals
NSCF	Non Self-consistent Field
OA	Oleic Acid
PBE	Perdew-Burke-Ernzerhof
PL	Photoluminescence
PXRD	Powder X-Ray Diffraction
rh	Rhombohedral
SPR	Surface Plasmon Resonance
SCF	Self-consistent Field
TCOs	Transparent Conducting Oxides
TEM	Transmission Electron Microscopy
TIO	Titanium-doped Indium Oxide
UV-Vis-NIR	Ultraviolet-Visible-Near-Infrared Spectroscopy
VB	Valence Band
XPS	X-ray Photoelectron Spectroscopy

Chapter 1 Introduction to Semiconductors and Indium (III) Oxide

A semiconductor has an electrical conductivity between a conductor and an insulator. A wide range of conductivities observed in different materials are dependent on the band gap which refers to the energy difference between the top of the valence band (VB) and the bottom of the conduction band (CB). Materials with small band gaps are referred as semiconductors while those with larger band gaps (> 4eV) are insulators. Conductors either possess very small band gap or no band gap at all, resulting from an overlap of the VB and CB. Electrons in the semiconductor can be excited from the VB to the CB when sufficient energy is applied.[1]

An intrinsic semiconductor is a pure semiconductor without intentionally doped impurities, whose charge carriers are determined by the material itself mainly arising from crystallographic defects. However, an extrinsic semiconductor is generated by aliovalent doping of the corresponding intrinsic semiconductor.[2] Moreover, these impurities can be classified as either donors or acceptors based on their energy level in the band gap. Donor impurities with energy levels near the CB of the semiconductor can provide the extra electrons to form an n-type semiconductor. By contrast, acceptor impurities are able to accept electrons from the VB, resulting in positively charged holes forming a p-type semiconductor, where the apparent flow of holes can be achieved in the VB by electrons hopping between the holes.[2] The band structure of n-type and p-type semiconductors are demonstrated below in Figure 1.1.

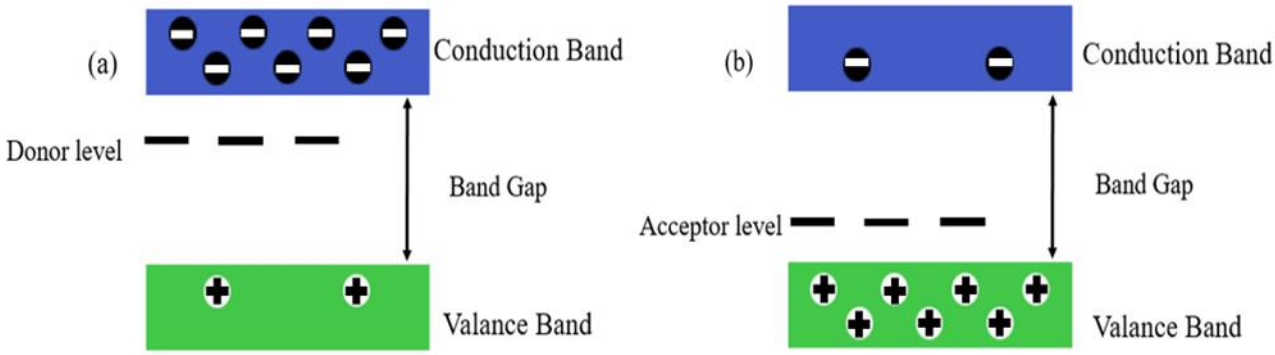

Figure 1.1: Illustration of band structure for (a) n-type semiconductor with donor level and (b) p-type semiconductor with acceptor level. Dark circles and light circles represent electrons and holes, respectively.

Unique physical properties of transparent conducting oxides (TCOs) have attracted considerable attention for the application in devices.[3] The key features of the TCOs include transparency as well as electrical conductivity similar to those of metallic compounds.[4]

In_2O_3, in particular, is an intrinsic n-type TCO with a wide band gap (~3.75 eV) combined with high charge carrier concentration and mobility.[5-6] Hitherto, it has been widely exploited in various fields, such as batteries, solar cells, electrodes, displays, sensors *etc.*[7-9] In_2O_3 is a polymorphic semiconductor with two distinctly different phases, a stable body-centered cubic bixbyite-type structure (bcc-In_2O_3) and a metastable corundum-type rhombohedral structure (rh-In_2O_3).[3]

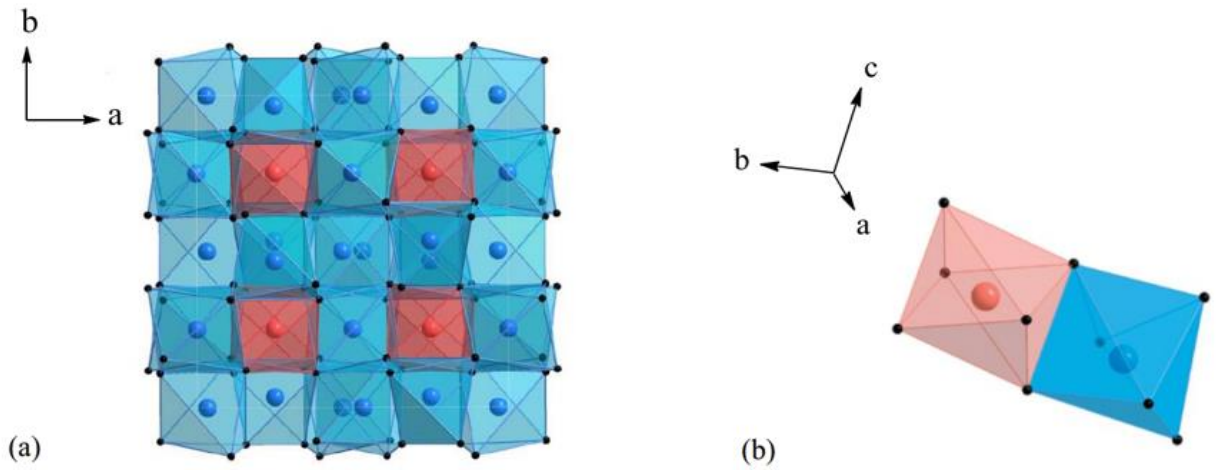

Figure 1.2: The body-centered cubic bixbyite-type structure of In_2O_3 (a) unit cell and (b) the b-sites (red) and d-sites (blue) within the structure. Large blue and red spheres indicate indium ions and oxygen ions are indicated by small black spheres.[3]

The thermodynamically stable form of In_2O_3 is cubic bixbyite (bcc-In_2O_3) which is a deviation of the fluorite structure obtained by removing one-fourth of the anions, and slightly offsetting the positions of the remaining anion sites (Figure 1.2(a)).

Consequently, In^{3+} cations can exist in two characteristic locations, known as b-sites and d-sites (Figure 1.2(b)). One-fourth of indium cations at the b-sites are slightly trigonally compressed octahedral (D_{3d} point group) while three-fourths of indium cations at the d-sites reside in highly distorted six-coordinate sites (C_2 point group).[10] Since the symmetry of the b-sites and d-sites is different, cations in these positions are likely to possess distinct spectroscopic properties.

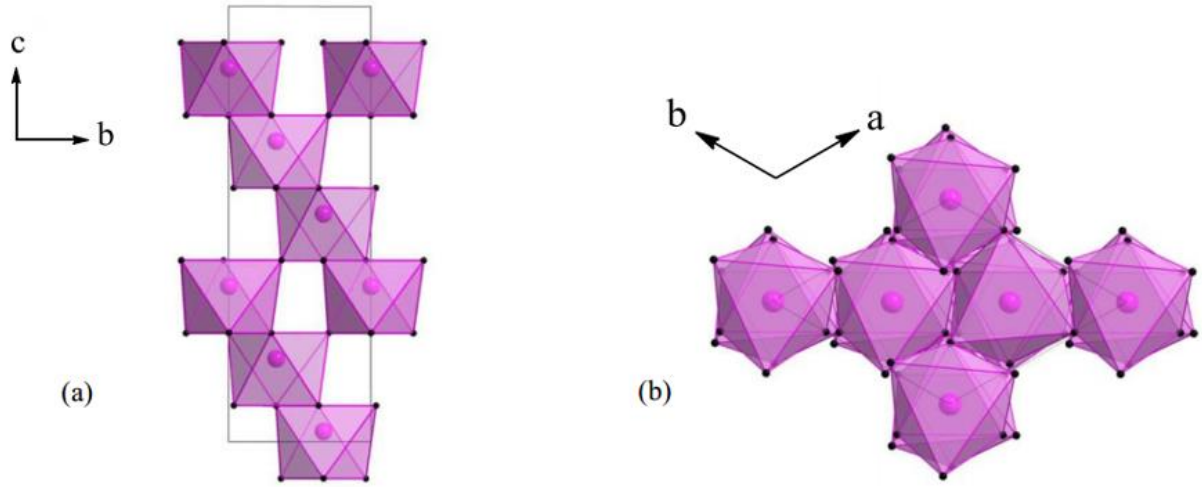

Figure 1.3: The metastable rhombohedral structure of In_2O_3 viewed along a-axis (a), and c-axis (b). Indium atoms are depicted as purple spheres and oxygen atoms are shown as black spheres.[3]

The metastable rhombohedral corundum-type In_2O_3 obtained at high pressures or temperatures is not common.[11] As shown in Figure 1.3, the structure of the rh-In_2O_3 belongs to the hexagonal crystal family consisting of hexagonal close-packed oxygen ions,[12] where In^{3+} ions are located in two-thirds of the six-coordinated cationic C_{3v} sites. In addition, rh-In_2O_3 NCs exhibit distinct photoluminescence (PL) properties from those of the bcc-In_2O_3 species which mainly stem from fewer structural defects in the bcc NCs.[13] Hence, it is of great significance to explore the stabilization of the rhombohedral phase due to its unique physical properties.

1.1 Phase Transformations of Indium (III) Oxide

Previous research by Farvid *et al.*[13] has demonstrated that the phase transformation from rh-In_2O_3 to bcc-In_2O_3 occurs along with increasing particle size during the synthesis of colloidal In_2O_3.The phase transformation of In_2O_3 NCs is correlated with a critical size of 5 nm in diameter. Particles with size equal to or less than 5 nm tend to be rhombohedral while those larger than 5 nm are cubic bixbyite.[3] The In_2O_3 NCs with smaller particle sizes prefer to adopt the metastable rhombohedral phase rather than cubic bixbyite. It is well known that the thermodynamic phase stability of solids can be spontaneously reversed below a critical size. Essentially, the reversal of the phase stability in nanocrystalline materials stems from the large surface to volume ratios in reduced dimensions. The high surface area of nanostructures can serve to stabilize metastable phases spontaneously due to contributions from size-dependent surface energy and surface stress.[13-15] Additionally, the concentration of charges on the surface will also affect the phase stability of the small particles. A compressive surface stress on the particle results in the electrostatic repulsion between surface charges and leads to the increase of interatomic distances.[3] Since the structure of rh-In_2O_3 is more densely packed than that of bcc-In_2O_3 by ca. 2.6%, rh-In_2O_3 is much more energetically favorable and stable at smaller NC sizes.[3]

The direct phase transformation between rh- and bcc-In_2O_3 nanostructures has been reported when high pressure and temperature were applied to bcc-In_2O_3. The phase change from cubic to rhombohedral occurs at 65 kbar and 1250 °C.[11] The harsh reaction conditions required to obtain rh-In_2O_3 is often not favorable and hence, mild colloidal synthesis is preferred. For instance, In_2O_3 NCs can be formed from indium(III) acetylacetonate ($In(acac)_3$) precursors via a hydrolysis mechanism at ambient pressure and temperature greater than 200 °C (Figure 1.3). Previous studies

have demonstrated that the intermediate indium oxyhydroxide (InOOH) is synthesized and that both rhombohedral and cubic phase coexist during the reaction.[3] Water plays a key role in the hydrolysis process. However, it must be present in controlled and minimal amounts so as to obtain the transitory rhombohedral phase. Comparatively, a large amount of water will lead to a much more rapid nanocrystal growth, and only cubic phase NCs can be obtained.[3] Taking into account that the reaction is carried out under an inert atmosphere of argon, the main proportion of oxygen in the In_2O_3 is assumed to originate from the acetylacetonate of the precursor whereas the water here is just to initiate the nucleation step of the reaction.[16]

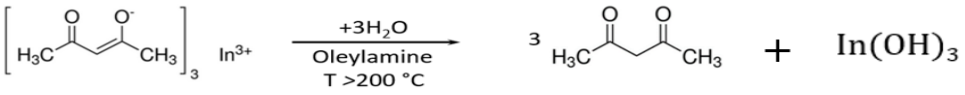

(1)

$$In(OH)_3 \xrightarrow{-H_2O} InOOH \quad (2)$$

$$2InOOH \xrightarrow{-H_2O} rh\text{-}In_2O_3 \quad (3)$$

$$rh\text{-}In_2O_3 \rightarrow bcc\text{-}In_2O_3 \quad (4)$$

Figure 1.3: Hydrolysis mechanism of In_2O_3 formation from $In(acac)_3$ precursors.

Controlling the phase structure of In_2O_3 NCs during the synthesis plays a key role in manipulating the electronic and optical properties of pure and doped In_2O_3 NCs. For instance, broad plasmon band is observed only for Sn-doped In_2O_3 NCs with bcc phase in the near-infrared (NIR) region rather than those with rh phase.[17] It is suggested that rational selections of dopant precursors and strict controlling of the reaction conditions are central to synthesizing the phase-controlled doped In_2O_3 NCs.

1.2 Synthesis of Doped Semiconductor Nanocrystals

It is well known that electronic and optical properties of semiconductor can be changed greatly by doping and adopting different strategies for synthesis. Colloidal synthesis can be utilized to synthesize NCs with well-controlled size, shape, composition and crystal phase.[18] A variety of approaches have been explored to synthesize doped colloidal semiconductor NCs. Hot-injection is one method where a dopant precursor is injected dropwise to a hot reaction mixture in order to obtain increasing doping levels. Sol-gel is another method which is widely used for the preparation of metal oxides where monomers are converted into a colloidal suspension (sol) as the precursor for an integrated network (gel). Given the effect of the nanocrystal surface ligand exchange, a significant proportion of the dopants, even under mild reaction, can reside on the nanocrystal surface.[19] Hence, the most common method to incorporate dopants in the substitutional sites of the host lattice is to include a dopant precursor at the beginning of the synthesis, which is known as one pot colloidal synthesis.[20]

Although doped semiconductor NCs reveal very promising results, there are still some concerns with respect to doping concentration level and distribution of dopant ions. Low doping concentrations have been reported for doped II-VI NCs, which have been the most widely studied host lattices.[21] Further thermodynamic and kinetic study regarding dopant incorporation in the nanocrystal can be used to explain the incorporation mechanism in these materials. Moreover, in order to confirm whether or not the dopant is uniformly distributed in the host lattice, careful characterization should be done for the resulting NCs.[22] Here, spectroscopic techniques are used as powerful tools to identify successful doping.[23] For example, optical absorption spectroscopy of

Co-doped CdS and ZnS NCs has been used to demonstrate that electronic transitions are sensitive to the local environment and utilized to confirm doping of Co in NCs.[21]

1.3 Mechanisms of Doped Semiconductor Nanocrystals

Several mechanisms have been proposed to explain doping in semiconductor NCs. One possible mechanism is self-purification.[22] This model emphasizes the thermodynamic perspective indicating that NCs are hard to dope as much higher energy is required to enable the impurities to be inserted into smaller NCs than larger ones.[23] Moreover, impurities are easily expelled from the NCs, owing to the short distance a defect or impurity must travel from inside to the surface of a nanocrystal.[24] However, this view is based on the assumption of thermodynamic equilibrium, which is strongly determined by the diffusion of impurity atoms. It can be only applied to those NCs synthesized at high temperature with rapid dopant diffusion. However, colloidal synthesis is performed at relatively lower temperature with slower dopant diffusion.[22] It has been demonstrated that in this case, kinetic factors are much more important than thermodynamic diffusion to govern the dopant incorporation process. Hence, the trapped dopant model is proposed based on a kinetic assumption, where the dopant incorporation in the NCs is controlled by the adsorption of impurities on the nanocrystal surface during the growth (Figureb1.4).[22] This model suggests that nanocrystal shape, surface morphology, and surfactants are the main factors that control dopant incorporation and that surface energies can be used to choose possible dopants in the NCs.[21]

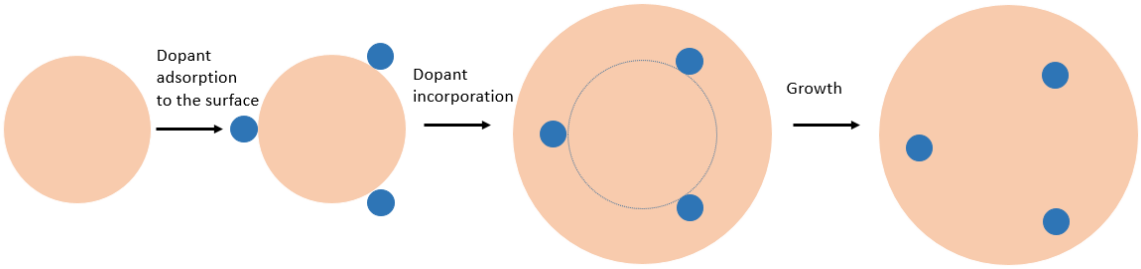

Figure 1.4: The scheme of trapped dopant model for doped semiconductor nanocrystals.

1.4 Plasmonic Properties of Doped Semiconductor Nanocrystals

In physics, surface plasmon resonance (SPR) is defined as the resonant oscillation of electrons stimulated by incident light when the frequency of incident photons matches the natural frequency of surface electrons.[25] SPR in doped semiconductor NCs has attracted significant interest, owing to its potential applications in spectroscopy, biological sensing, biomedicine, and nano-optical devices.[26] For instance, SPR can lead to the generation of a strong optical field near the surface of NCs, which is used to enhance signals in modern high-sensitivity spectroscopic techniques, including surface-enhanced Raman spectroscopy (SERS).[27] Optical field-enhanced light absorption is also conducive to the application of plasmonic NCs as light concentrators in photovoltaics cells.[28]

SPR of a nanocrystal can be tuned by variation of the size, shape, composition, and surrounding medium.[29] It is noted that traditional noble metals such as gold and silver nanostructures can exhibit SPR in the visible-to-Near-Infrared (Vis-NIR) region.[30] However, a series of TCOs mainly show the plasmon resonance in NIR and MIR, due to the relatively lower plasma energy.[31] The mechanism for TCOs is the same as those for noble metals, despite the fact

that TCOs have lower charge carrier concentration ($n \approx 10^{21}$ cm^{-3}) than that of typical metals ($n \approx 10^{23}$ cm^{-3}).[32]

Furthermore, both plasmon absorption intensity and energy are correlated to free carrier concentration in TCO NCs that can be quantitatively described by Drude-Lorentz theory,[33] which was originally developed as a model of the free electron gas in metals. According to this model, the absorption coefficient (α) is directly proportional to the charge carrier concentration (*N*),[34] based on the following eq 1.1 where *e* is the electron charge, *m** is the effective mass of an electron, ε_0 is the vacuum permittivity, τ is the mean free time between two electron scattering events, *n* is the refractive index of an undoped semiconductor, and *c* and ω are the speed and frequency of light, respectively.

$$\alpha_{\text{free electrons}} = \frac{Ne^2}{m*\varepsilon_0 nc\tau\omega^2} \quad 1.1$$

$$\omega_{\text{p}} = \sqrt{\frac{Ne^2}{m^*\varepsilon_{opt}\varepsilon_0}} \quad 1.2$$

In eq 1.2, $\varepsilon_{\text{opt}} = n^2$ is a dielectric constant measured in the transparent region of the spectrum of an undoped semiconductor. This equation explains the trends that the energy position of the plasmon band, ω_{p}, has a square root dependence on the free electron concentration and also is associated with the refractive index of the surrounding medium.[35] It is believed that broadly tunable SPR of TCOs can be realized because carrier densities of semiconductors can be varied from 10^{16} cm^{-3} to 10^{21} cm^{-3}, most commonly by means of doping.[29] In contrast, carrier concentrations in noble metals, such as gold and silver are large and difficult to change appreciably,

and Au and Ag NCs have loss of optical absorption due to electronic transitions in the visible range.[26] Furthermore, the high cost of noble metals limits practical applications.[36]

Previous studies have shown that tin doped In_2O_3 (ITO) NCs have been successfully synthesized and the SPR absorption of ITO NPs can be easily tuned from 1618 nm to >2200 nm by changing the concentration of the Sn doping from 3% to 30%.[26] SPR of antimony-doped tin dioxide NCs has been investigated, exhibiting a strong absorption band in the visible edge of ending to NIR region.[37]

Recently, increased interest of SPR has been extended to the MIR due to its significant potential across a wide range of applications, such as chemical sensing, thermal imaging, enhanced spectroscopy, and more speculatively heat scavenging.[38] Previously, detectors fabricated with traditional metal-based materials are inherently subject to several drawbacks, such as fixed resonance, bad compatibility as well as large metal loss. Although new InAs heterostructures and graphene are fabricated with reduced loss and improved confinement for applications in the MIR[39-40], doped TCO NCs have apparent advantages over these materials, such as the low cost, well-controlled size of the NCs, stability and durability, and easy self-assembly.

So far, antimony-doped In_2O_3 (AIO) NCs and titanium-doped In_2O_3 (TIO) NCs have not been explored. In this thesis, I examined the tunability of the plasmon resonance of both newly doped In_2O_3 NCs in the MIR as new well-controlled material systems for exploring the science of plasmonics.

1.5 First-principles Simulation Method in Material

First-principles simulation, using density functional theory (DFT) calculations with plane waves and pseudopotentials, has become an advanced technique in condensed matter, building a

model of a real system of material and exploring its electronic structure and related optical properties.[41]

Among different simulation codes, QUANTUM ESPRESSO has been widely used for electronic-structure calculations and materials modeling due to its free open-source software, well developed and tested electronic structure codes as well as user friendliness.[42] As an integrated suite of computer codes, QUANTUM ESPRESSO stands for the *opEn-Source Package for Research in Electronic Structure, Simulation, and Optimization.*

Based on the DFT, a variety of methods and algorithms are included in the QUANTUM ESPRESSO to realize a chemically realistic modeling of materials, using plane wave basis sets and pseudopotentials to represent electron–ion interactions.[43] Given the utilization of the periodic boundary conditions, QUANTUM ESPRESSO can thus be applied in any crystal structure, supercell, metals as well as insulators at the nanoscale. Aside from the electron-ion interactions of the material, the exchange and correlation energy terms in DFT methods should also be taken into account. In this project, Perdew-Burke-Ernzerhof (PBE) of generalized gradient approximation (GGA) are used as the gradient-corrected exchange and correlation functionals to improve the performance of calculation of doped In_2O_3 NCs.

1.6 Motivations and Scope of the Thesis

As mentioned previously, In_2O_3 is an intrinsic n-type semiconductor with a high free carrier concentration and mobility, which can be employed as the host lattice for doping. New dopants, Sb and Ti, are used to synthesize the doped In_2O_3 NCs and to mainly explore the tunability of the plasmon resonance in the MIR.

The first part of this work is associated with synthesizing AIO NCs, controlling and elucidating the tunability of SPR in the MIR as well as investigating the structure and morphology, with respect to the doping concentration of the precursor. In addition, AIO NCs could pose an interesting direction to be explored due to the possibility of mixed oxidation states of Sb. The second section of this research focuses on the synthesis of TIO NCs and exploration of the tunability of plasmon in the MIR. Besides, the influence of the size of TIO NCs on the plasmon was also studied, by using different synthetic temperatures to control the growth of NCs.

In the case of both projects, a variety of characterization methods were performed for as-synthesized AIO and TIO NCs in order to obtain the corresponding structural information as well as the electronic and optical properties. The simulation code, QUANTUM ESPRESSO was applied to deliver more information and details for further elucidation of electronic and optical properties of AIO and TIO NCs. Further post-synthesis treatment, like fast annealing under H_2, was conducted to modify and enhance the quality of the plasmon of as-synthesized NCs.

It is expected that newly synthesized AIO and TIO NCs can be added to the current database of plasmonic nanomaterials and provide further insight into how different dopants alter the plasmonic features of the same host lattice. In addition, broadly tunable plasmon of AIO and TIO NCs can be employed in potential applications, such as the sensing, enhanced spectroscopy, and thermal imaging.

Chapter 2 Experimental Methods

2.1 Materials

All chemical reagents and solvents were used as received from the manufacturer without further purification. Indium acetylacetonate ($In(acac)_3$; 98%) and Titanium (IV) isopropoxide ($Ti(O\text{-}i\text{-}Pr)_4$, 98%) were purchased from Strem Chemicals. Antimony (III) chloride ($SbCl_3$; 99%) and oleylamine (70%) were obtained from Sigma Aldrich. Oleic acid (90%) was purchased from Aldrich. Toluene (EMD Chemicals; 99.9%), hexane (Fischer Scientific; 98.5%) and absolute ethanol were used as solvents.

2.2 Synthetic Methods

2.2.1 Synthesis of Antimony-doped Indium Oxide Nanocrystals

The synthesis of antimony-doped indium oxide (AIO) NCs was carried out according to the modified procedure outlined by Wang *et al*.[13] In a typical reaction, 0.9 g of $In(acac)_3$, 7.2 g of oleylamine, and varying amounts of $SbCl_3$ were mixed in a 100 mL three-neck round-bottom flask under the flow of argon. The mixture was heated to 250 °C within one hour and proceeded to react for another one hour with constant stirring at the same temperature. After the reaction, the mixture was then cooled to room temperature and precipitated by centrifugation at 3000 rpm for 10 min. The precipitate was washed with ethanol, and similar procedures were repeated two more times for further cleaning.

Subsequently, 1.5 mL oleic acid (OA) was added to the obtained sample, and the mixture was stirred at 90 °C oil bath for half hour followed by precipitation with ethanol. This ethanol washing process was repeated three times to remove the surface-bound dopant ions and additional oleic acid. Finally, a part of the sample was dried and crushed for XRD measurement, and the remainder was dispersed in a nonpolar solvent, like hexane and toluene for other measurements.

2.2.2 Synthesis of Titanium-doped Indium Oxide Nanocrystals

Titanium-doped indium oxide (TIO) NCs were synthesized following a similar method as shown above. The only difference here was that specific volume of titanium (IV) isopropoxide should be quickly injected into the solvent, oleylamine, so as to avoid the hydrolysis of the dopant during the sample weighing. All similar procedures were then performed under identical conditions for the synthesis and post treatment of the NCs.

2.3 Characterization Techniques

2.3.1 Powder X-ray Diffraction (PXRD)

PXRD is a powerful tool to identify the crystal structure of materials. In addition, the crystallite size can also be estimated through the Scherrer equation:

$$L_{hkl} = \frac{K\lambda}{Bcos(\theta)} \quad 2.1$$

L_{hkl} is the crystallite size regarding diameter in nm and K is the dimensionless shape factor, typically equal to 0.9. λ is the wavelength of the X-rays and B is the full width at half-maximum (FWHM), and θ is the diffraction angle in radians.[44]

The measurements were carried out with an INEL XRD diffractometer, utilizing monochromatic Cu-Kα radiation (λ = 1.5406 Å) in Dr. Holger Kleinke's group in Department of Chemistry at the University of Waterloo.

2.3.2 Transmission Electron Microscopy (TEM)

TEM can be usually used to confirm the morphology and particle size of NCs. For measurement, a small portion of colloidal solution was deposited on copper grids with lacey Formvar/carbon support films purchased from Ted Pella, Inc. TEM images were then collected by the JEOL-2010F microscope operating at 200 kV at McMaster University. Gatan Digital Micrograph software was used to measure the d-spacing from high-resolution TEM (HRTEM) images to confirm the crystal structure. In addition, the ancillary equipment, Energy Dispersive X-ray (EDX) was employed to characterize the elemental composition of the sample with the probing energy in the range from 0 keV to 2 keV.

2.3.3 X-ray Photoelectron Spectroscopy (XPS)

XPS is a surface-sensitive technique that is commonly utilized to determine the composition of the sample and the oxidation states of the elements. XPS spectra are obtained by probing the kinetic energy of the photoelectrons ejected by X-ray radiation from the surface of the sample.

In this project, XPS measurements were performed using a Thermo-VG Scientific ESCALab 250 microprobe equipped with a monochromatic Al Kα source (1486.6 eV) in WATLab at the University of Waterloo. Peak fittings for the XPS spectra were conducted by the Casa XPS software.

2.3.4 Raman Spectroscopy

Raman spectroscopy is commonly utilized to provide information about the vibrational modes of the material based on the inelastic scattering of monochromatic laser light. The shift in laser photon frequency can be observed due to the interaction of the light photon with the molecular vibrations, phonons or other excitations in the system. In addition, the vibrational information can be associated with the strength, length and the arrangement of the chemical bond[45].

In this project, Raman spectroscopy is mainly used to confirm the effect of the dopant on the vibrational modes of the indium oxide NCs. Raman spectra were recorded at room temperature using a Renishaw 1000 spectrometer with the Ti-sapphire laser emitting at 785 nm. Furthermore, 10% of the total output power (40mW) was employed as the radiation source. Prior to the measurement, the spectrometer was calibrated using a silicon foil.

2.3.5 Ultraviolet-Visible-Near-Infrared (UV-Vis-NIR) Spectroscopy

UV-Vis-NIR spectroscopy is a valuable technique to determine the electronic absorption range for doped semiconductor NCs. It can also provide some information on their electronic structures and optical properties, such as the band gap transition, free-carrier absorption, *etc*.

UV-Vis-NIR absorption spectra were obtained using a Varian Carey 5000 UV-Vis-NIR spectrophotometer. In order to avoid the effect of the solvent at longer wavelength, solid-state UV-Vis-NIR absorption spectra were collected from 200 nm to 3200 nm with nanocrystal solution drop-casting on the quartz film.

2.3.6 Fourier Transform Infrared (FTIR) Spectroscopy

FTIR is a strong and powerful optical technique that can represent the fingerprint of a sample based on the frequencies of vibrations of the material. It can be employed to identify the organic molecules adsorbed on the surface of the NCs. Furthermore, doped semiconductors can show optical absorption in MIR region owing to the free-carrier plasmonic resonance. In this study, FTIR spectra were recorded from KBr pellet in absorption mode ranging from 400 to 4000 cm^{-1} on the FTIR Bruker Tensor 37 in Dr. Linda Nazar's group in Department of Chemistry at the University of Waterloo. Furthermore, quantitative analysis of the intensity of the plasmonic band can be carried out with an appropriate normalization method based on the phonon vibrations of the nanocrystal.

Chapter 3 Studies of Structures and Optical Properties in Antimony-doped Indium Oxide Nanocrystals

3.1 Crystal Structure and Morphology of AIO NCs

Colloidal AIO NCs were synthesized at 250 °C as described in section 2.2. Figure 3.1 shows the XRD patterns of the as-synthesized samples with various doping concentrations. It can be observed that all the main diffraction peaks of the synthesized samples match the bulk bcc-In_2O_3 reference pattern very well. The average particle size, obtained from the Scherrer equation, is estimated to be ca. 10 nm for samples with [Sb]/[In] ratio below 0.10. In addition, sharper peaks are observed for samples with the higher doping ratio, 0.10 and 0.15, indicating the large NC size of those samples.

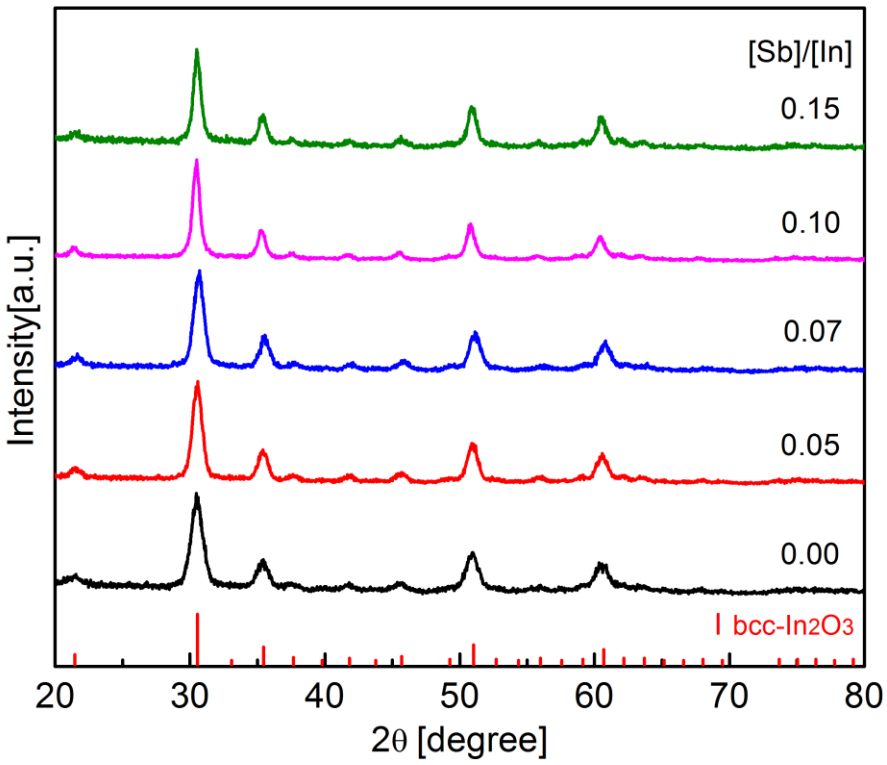

Figure 3.1: XRD patterns of Sb-doped In_2O_3 NCs, synthesized at 250 °C with different starting [Sb]/[In] ratios indicated in the graph. Red lines at the bottom correspond to the XRD pattern of bulk bcc-In_2O_3 (JCPDS 06-0416).

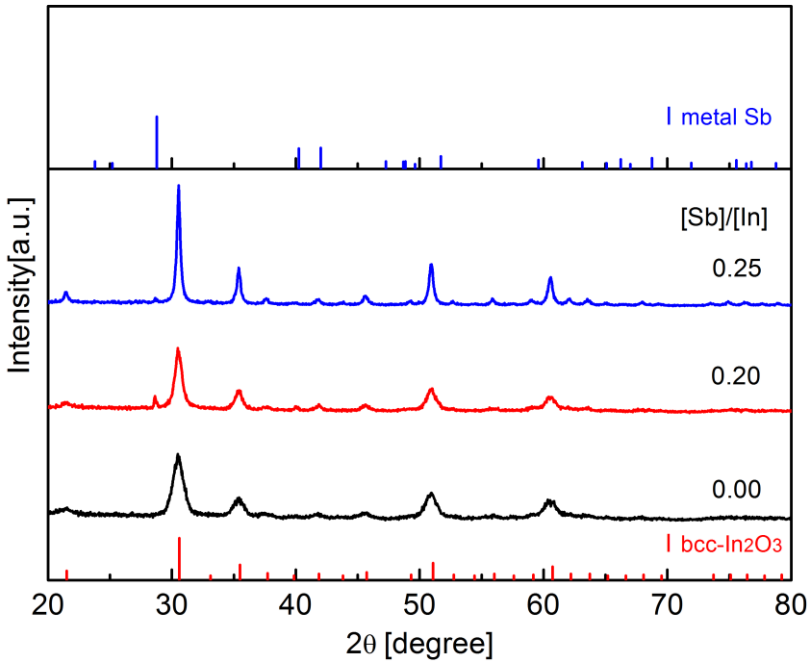

Figure 3.2: XRD patterns of pure and heavily Sb-doped In_2O_3 NCs with starting [Sb]/[In] 0.20 and 0.25, respectively. Red lines (bottom) indicate the pattern of bulk bcc-In_2O_3 while blue lines (top) refer to the pattern of metal Sb.

However, for those heavily doped AIO NCs with the [Sb]/[In] ratio, such as 0.20 and 0.25, one small peak appears at approximately 28 degrees which can be assigned to the phase of metal antimony. To further confirm this impurity, metal antimony was synthesized with the same strategy used for the synthesis of doped In_2O_3 NCs**.** The XRD pattern of as-synthesized metal antimony is in good agreement with that of bulk antimony (Figure A1). The appearance of secondary phase indicates that incorporation of dopant Sb into the host lattice and formation of

elemental Sb are competing processes above critical doping ratio, 0.20. Two possible reasons may account for this observed phenomenon. One is the disproportionation of Sb^{3+} ions, which can form Sb^{5+} ion as well as metal Sb. The second is that the solvent oleylamine used in the reaction can donate electron to the cation at elevated temperature, which facilitates the formation of metal Sb from the precursor Sb^{3+}.[16]

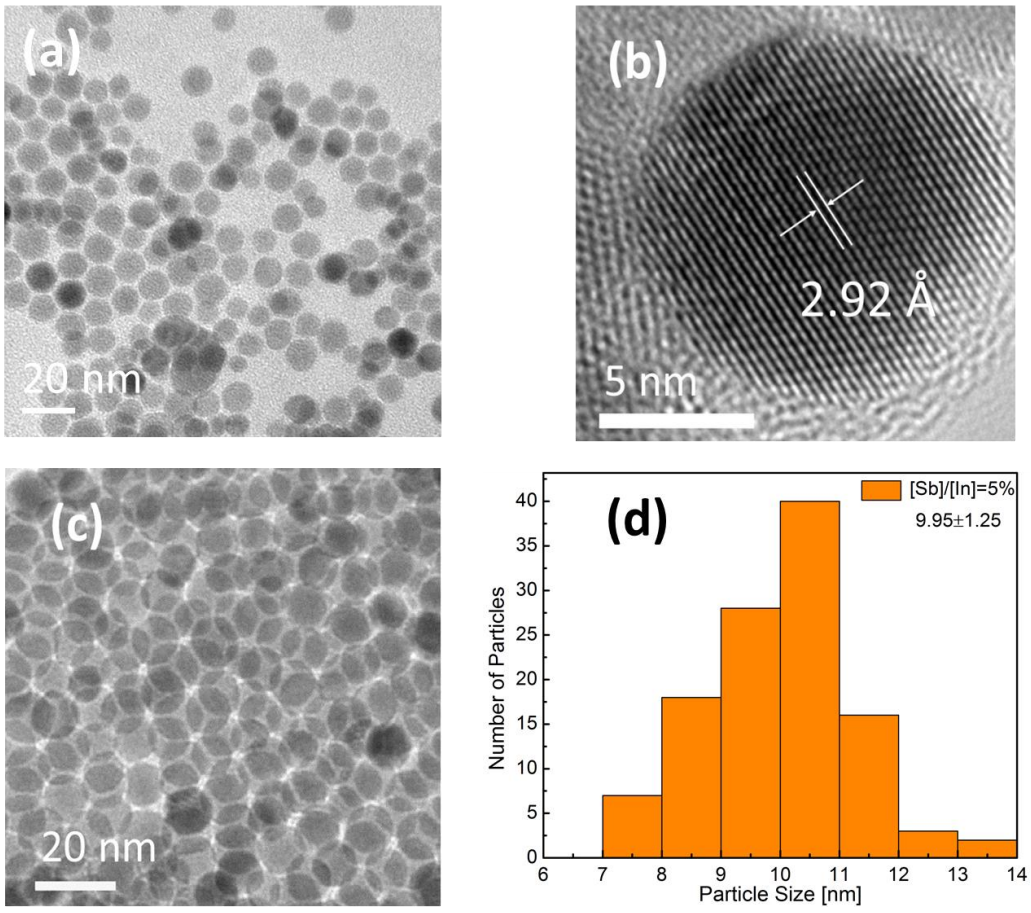

Figure 3.3: Representative TEM images of 5% AIO NCs. (a) Overview TEM image of AIO NCs. (b) HRTEM image of a single NC. (c) The well self-assembled double layers of AIO NCs, (d) The size distribution of AIO NCs.

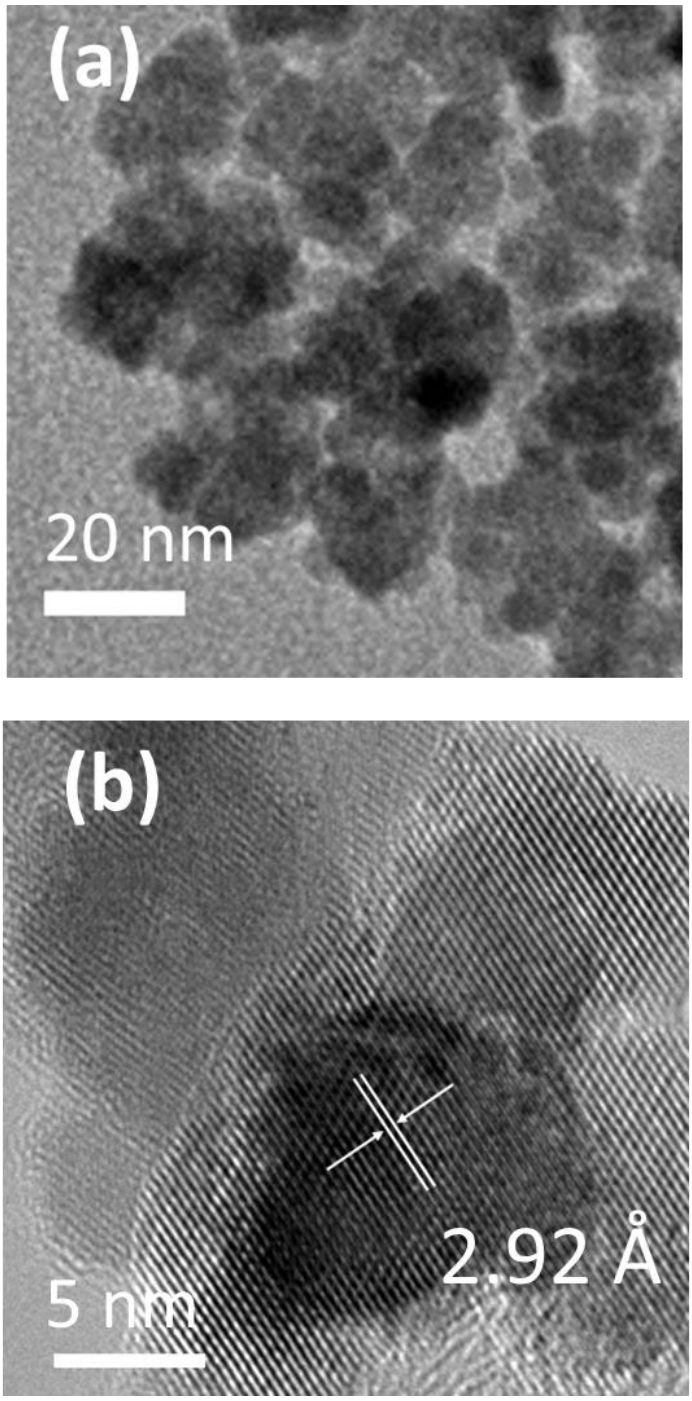

Figure 3.4: (a) Representative overview TEM image of AIO NCs with starting [Sb]/[In]=15% and (b) HRTEM image of a typical flower-like cluster resulting from the oriented attachment of AIO NCs.

Figure 3.3 (a) shows an overview TEM image of 5% AIO NCs deposited on carbon-coated Cu grids. It can be observed that these NCs have a spherical shape and a relatively narrow size distribution, with an average particle size of 9.95± 1.25 nm, which is consistent with the calculated value by the Scherrer equation from the XRD patterns. Notably, the HRTEM image demonstrates the clear lattice fringes of a single NC, which confirms the single crystalline nature of the AIO NCs. The measured lattice spacing of AIO NC in Figure 3.3 (b) is ca. 2.92 Å, corresponding to the plane (222) of bulk bcc-In_2O_3.[12] Image 3.3 (c) shows that these AIO NCs can be self-assembled well into uniform layers, owing to the narrow size distribution of nanoparticles.

Figure 3.4 (a) represents the flower-like clusters with the size of ca. 25 nm for AIO NCs synthesized with doping ratio of 15%. Importantly, oriented attachment is found extending over a number of NCs, with approximately the same d-spacing value, 2.92 Å shown in Figure 3.4 (b), which reveals that nanoflowers are formed from the assembly of these smaller bcc AIO NCs. Here, $SbCl_3$ is employed as the precursor for the synthesis of AIO NCs. For high doping ratio, [Sb]/[In]=15%, more Cl^- ions are present in the reaction and adsorb on the surface of the initially formed AIO NCs, which may facilitate the formation of the nanoflowers owing to the decreased surface protection of the solvent, oleylamine[46].

3.2 Elemental Analysis of AIO NCs

To determine the precise composition as well as the oxidation states of Sb dopants, XPS measurement was conducted on AIO NCs with different starting concentrations of Sb. Energy calibration was performed at the binding energy of 285.0 eV to avoid charge compensation. A representative XPS survey spectrum for AIO NCs synthesized with [Sb]/[In] = 10% is shown in Figure 3.5 (a).

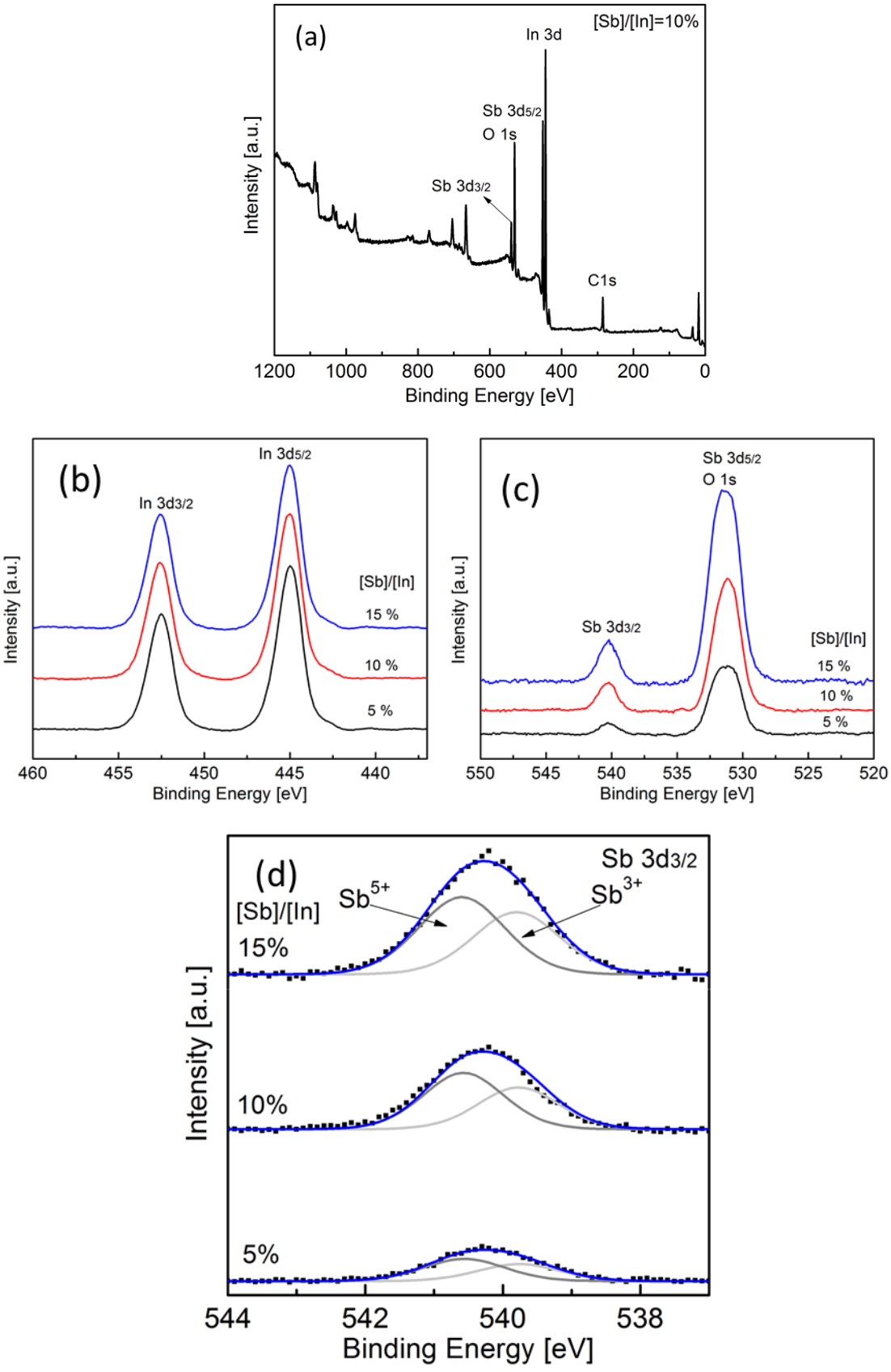
(a)
[Sb]/[In]=10%
In 3d
Sb 3d5/2
O 1s
Sb 3d3/2
C1s
Intensity [a.u.]
1200 1000 800 600 400 200 0
Binding Energy [eV]
(b)
In 3d5/2
In 3d3/2
[Sb]/[In]
15 %
10 %
5 %
Intensity [a.u.]
460 455 450 445 440
Binding Energy [eV]
(c)
Sb 3d5/2
O 1s
Sb 3d3/2
[Sb]/[In]
15 %
10 %
5 %
Intensity [a.u.]
550 545 540 535 530 525 520
Binding Energy [eV]
(d)
[Sb]/[In]
Sb5+
Sb3+
Sb 3d3/2
15%
10%
5%
Intensity [a.u.]
544 542 540 538
Binding Energy [eV]

Figure 3.5: (a) Representative XPS survey spectrum for AIO NCs synthesized with [Sb]/[In] = 10%. High-resolution XPS spectra of In 3d region (b), Sb 3d and O1s regions (c) for AIO NCs with different doping levels. (d) The Sb $3d_{3/2}$ peak. The solid black squares in (d) depict the raw spectra and the solid blue lines are the results of peak fits for Sb^{5+} (540.6 eV, dark gray line) and Sb^{3+} (539.8 eV, light gray line).

Apart from a weak C 1s, resulting from the hydrocarbons adsorbed on the surface of the AIO NCs, the presence of Sb, In and O peaks are clearly observed in the survey spectra as expected from the chemical composition of Sb-doped In_2O_3 NCs. Figure 3.5 (b) displays the high-resolution XPS spectra of In 3d region for AIO NCs with various doping levels. The doublet peaks of In $3d_{3/2}$ and $3d_{5/2}$ are situated at ca. 452.4 and 444.9 eV, respectively.[47] Figure 3.5 (c) shows the Sb 3d and O 1s peaks for AIO NCs with different starting doping ratios labeled in the graph. The determined binding energies are 540.1eV for Sb $3d_{3/2}$, 531.8 eV for Sb $3d_{5/2}$, and 530.9 eV for O 1s, respectively.[48] It is clear that the peak intensity of the Sb $3d_{3/2}$ increases with increasing Sb concentration. Given the strong overlap of the latter two peaks, actual doping concentration of Sb was determined by the relative intensities of Sb $3d_{3/2}$ and In 3d peaks. The obtained actual concentrations of Sb in AIO NCs are listed in Table 3.1.

Table 3.1: Actual doping concentration of Sb in colloidal AIO NCs as determined by XPS

Starting Sb concentration ([Sb]/[In] at. %)	Sb concentration in AIO NCs (at. %)
5	2.9
7	5.5
10	7.9
15	11.8
20	16.5
25	20.2

It is observed that the actual concentration of Sb in AIO NCs is systematically lower, compared to the starting [Sb]/[In]. Furthermore, it is more likely that binding of indium cations on nucleated NCs are kinetically faster than that of antimony cations, resulting in the relatively lower reaction rate of dopant incorporation.

It is evident that antimony can exist in two oxidation states, Sb^{5+} and Sb^{3+} in the AIO NCs, whereas Sb^{5+} ion behaves as an electron donor, providing two electrons for each ion, while Sb^{3+} ion is inactive for doping as it is in the same oxidation state as In^{3+} ion. Careful consideration must be taken to deconvolute the superimposed peaks of $Sb3d_{3/2}$ owing to the narrow separation of binding energy, 0.8 eV between Sb^{5+} and Sb^{3+}. In Figure 3.5 (d), peak fits for Sb $3d_{3/2}$ demonstrate that peak area of Sb^{5+} is apparently larger than that of Sb^{3+}, by ca. 30%, proving that AIO NCs belong to the n-type doping semiconductor material.

3.3 Spectroscopic Studies of AIO NCs

3.3.1 Raman Spectra of AIO NCs

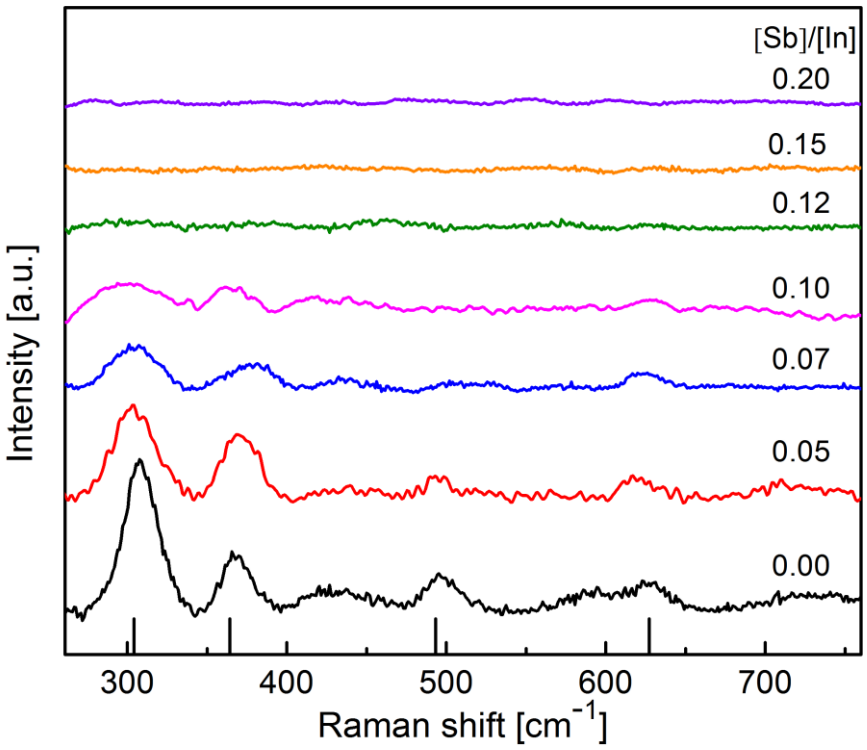

Figure 3.6: Raman spectra of AIO NCs with different doping concentrations indicated in the graph. Black lines at the bottom refer to the Raman peaks of bulk bcc-In_2O_3.

The crystal phase of the AIO NCs was further investigated by Raman spectroscopy, which can provide structural information for crystalline samples. Figure 3.6 displays Raman spectra of AIO NCs with different doping concentrations. Four Raman peaks for undoped In_2O_3 NCs are located at 307, 366, 497 and 630 cm^{-1}, resulting from the phonon modes of bcc-In_2O_3, and are in good agreement with the peaks (black lines) reported in the literature.[49] Compared to the spectrum of undoped In_2O_3 NCs, continuous weakening, and broadening of the characteristic peaks are observed for AIO NCs with increasing doping concentration ratio, up to 0.10. Furthermore,

intensites of theses peaks vanish completely with further increase in doping concentration. Although AIO NCs maintain the bcc crystal structure for all doped NCs, as identified by both XRD patterns and HRTEM images, weakening, broadening, and eventual disappearance of Raman peaks suggest the local crystal lattice distortion due to the incorporation of Sb ions into bcc-In_2O_3 NCs.

3.3.2 UV-Vis-NIR Absorption Spectra of AIO NCs

For UV-Vis-NIR absorption measurement, owing to the limitation of absorption in organic solvents, like hexane and toluene, solid-state UV-Vis-NIR was performed from 200 nm to 3200 nm. Here, colloidal solution of AIO NCs in toluene was drop-casted onto a quartz substrate and air-dried for the optical measurement. Figure 3.7 depicts the band-gap-normalized UV-Vis-NIR absorption spectra with different doping concentrations ([Sb]/[In]) indicated in the graph. For all absorption spectra, there is a shoulder around 300 nm, which is ascribed to the band gap absorption of semiconductor NCs.

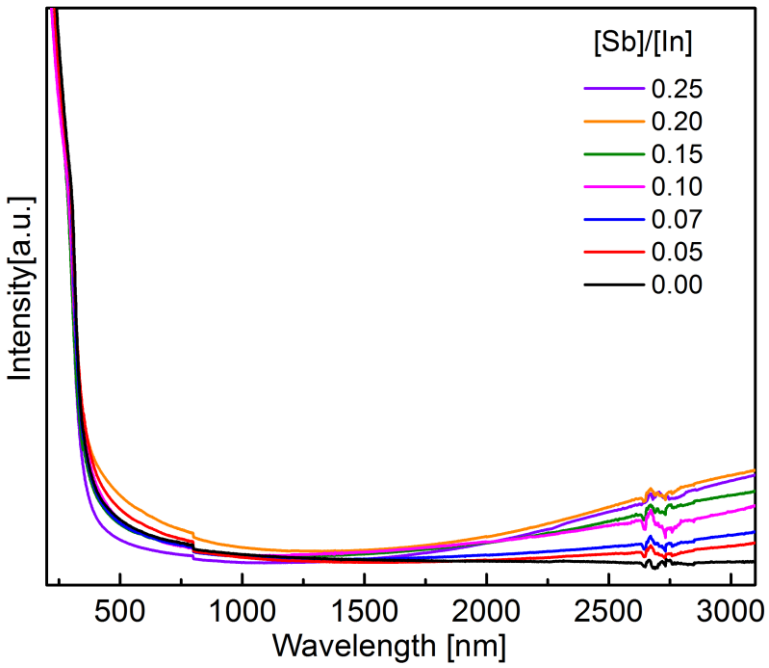

Figure 3.7: Band-gap-normalized UV-Vis-NIR absorption spectra of AIO NCs in the range from 200 nm to 3200 nm. Different doping concentrations ([Sb]/[In]) are indicated in the graph.

This band gap absorption is used to normalize all spectra so as to quantitatively compare plasmon resonance absorption of AIO NCs in NIR. The absorption intensities of AIO NCs in the NIR region increase gradually with increasing doping ratio, which indicates the increased electron concentrations introduced by doping. In the case of the 25% AIO NCs, absorption intensity drops back and is lower than that of 20% AIO NCs, due to the trap sites around the dopant ion, which decrease the free electron concentration.[50]

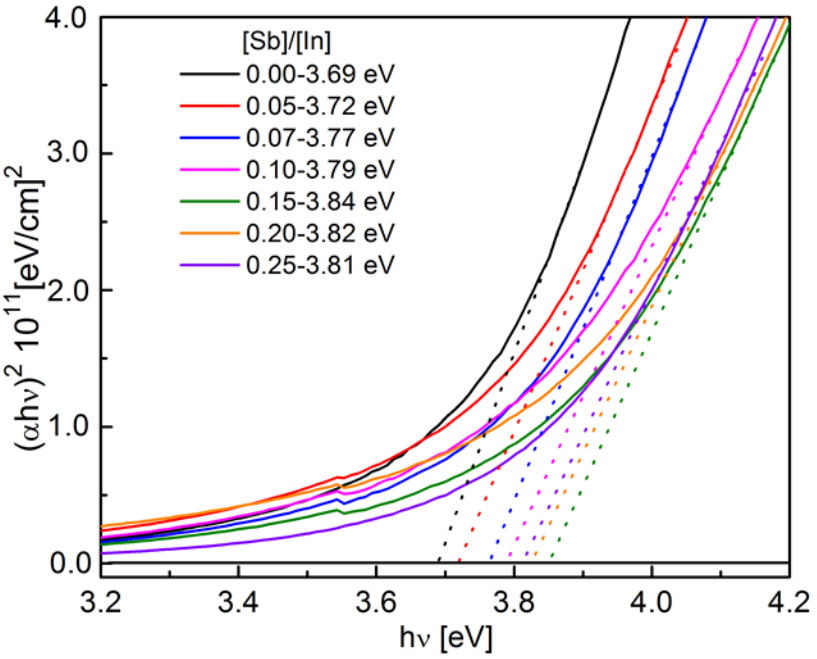

Figure 3.8: Tauc plot of optical band gap shift of AIO NCs with indicated various doping concentrations and corresponding band gap values.

Furthermore, the optical band gaps of AIO NCs with different doping concentrations were obtained from linear fits to Tauc plots of $(\alpha h\nu)^2$ versus the photon energy ($h\nu$) as depicted in the

Figure 3.8.[51] The determined optical band gap for pure In_2O_3 NCs is ca. 3.69 eV, which is in good agreement with the reported value found in literature.[5] The optical band gap of the AIO NCs shifts systematically to a higher energy as the increase of the number of electrons accumulating at the bottom of the conduction band, which is referred to as the Burstein-Moss effect.[52]

3.3.3 FTIR Absorption Spectra of AIO NCs

FTIR spectroscopy is a powerful and sensitive optical technique, which can be employed to identify the organic molecules and to record the absorption spectra of doped semiconductor NCs in the MIR, due to the free electron oscillation. Besides the absorption edge of plasmons of AIO NCs in the NIR, FTIR measurements were further conducted to obtain the complementary part of plasmon absorption for AIO NCs in the MIR. During sample preparation, unlike routine pellets made of KBr and target sample powder, transparent colloidal solution of AIO NCs in toluene was drop-casted onto pristine KBr pellet of well-controlled thickness and transparency so as to avoid scattering and allow for proper background subtraction. In particular, one schematic example of background subtraction for 7% AIO NCs is shown in Figure A2.

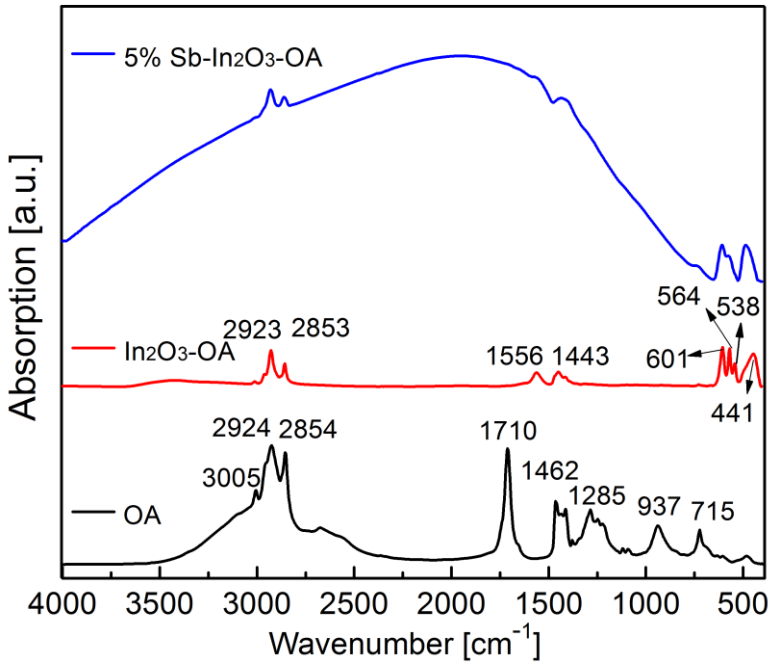

Figure 3.9: Representative FTIR spectra obtained from 5% Sb-In_2O_3-OA NCs (blue trace) , pure In_2O_3-OA NCs (red trace), and reference pure OA (black trace), respectively.

Figure 3.9 illustrates the representative FTIR spectra of In_2O_3 NCs (red trace), and pure oleic acid (OA, black trace). In the spectrum of OA, two sharp bands at 2924 and 2854 cm^{-1} can be assigned to the asymmetric and symmetric CH_2 stretch, respectively. The intense peak at 1710 cm^{-1} is derived from the existence of the C =O stretch, and the band at 1285 cm^{-1} indicates the presence of the C–O stretch. The O–H in-plane and out-of-plane bands appear at 1462 and 937 cm^{-1}, respectively.[53] In the case of In_2O_3 capped with OA (red trace), the asymmetric CH_2 stretch and the symmetric CH_2 shifted to 2923 and 2853 cm^{-1}, respectively. The observed red shift of the characteristic bands can be attributed to the adsorbed state of surfactants, which can be influenced by the field of the solid surface.[54] In addition, the disappearance of the C=O stretch band and the appearance of two new bands at 1556 cm^{-1} and 1443 cm^{-1} can be assigned to the characteristic

asymmetric (COO–) and symmetric (COO–) stretch, which strongly suggests that In_2O_3 NCs have been coated with OA successfully, as evidenced by the 5% Sb-In_2O_3-OA NCs (blue trace) as well.

In addition, four intense peaks at 601, 564, 538 and 441 cm^{-1} correspond to the In–O phonon vibration modes, which are characteristics of cubic In_2O_3.[55] The peak at 564 cm^{-1} is used to normalize all spectra for quantitative analysis of the plasmon absorption. It is proposed that the intensity of this peak should be proportional to the amount of In-O bonds and less affected by doping level and reaction temperature. All normalized spectra for AIO NCs with various doping ratios are shown in Figure A3.

There is a remarkable difference in the FTIR absorption spectra of undoped and 5% Sb-doped In_2O_3 NCs in Figure 3.9. Compared to the spectrum of the undoped In_2O_3 NCs, strong and broad plasmon absorption band is observed from ca. 650 cm^{-1} to 4000 cm^{-1} for the 5% Sb-doped In_2O_3 NCs, which can be attributed to the plasmonic resonance of free carriers excited by the MIR light. This is also consistent with the noticeable color difference of colloidal solution from colorless In_2O_3 NCs to greenish 5% Sb-doped In_2O_3 NCs. Consequently, the appearance of broad plasmon absorption in the MIR region is a signature of doping in the case of AIO NCs as generation of free carriers in the NCs can be evaluated by the optical properties.[56]

3.4 Analysis of the Plasmonic Properties of AIO NCs by Drude model

In the case of AIO NCs, the UV-Vis-NIR and FTIR absorption spectra are obtained in two different instruments with absorption intensity at different scales, which makes it challenging to analyze the spectra. In order to perform a rational analysis of the plasmon absorption for a series of AIO NCs, covering the optical range from NIR to MIR, normalized UV-Vis-NIR absorption

spectra in Figure 3.7 and FTIR spectra in Figure A3 are combined, on the basis of the overlapping portion of absorption from 2500 nm to 3200 nm. More details about this data processing are exemplified in Figure A4. The resulting normalized spectra of AIO NCs are present in Figure 3.10 (a), together with the corresponding analysis in Figure 3.10 (b).

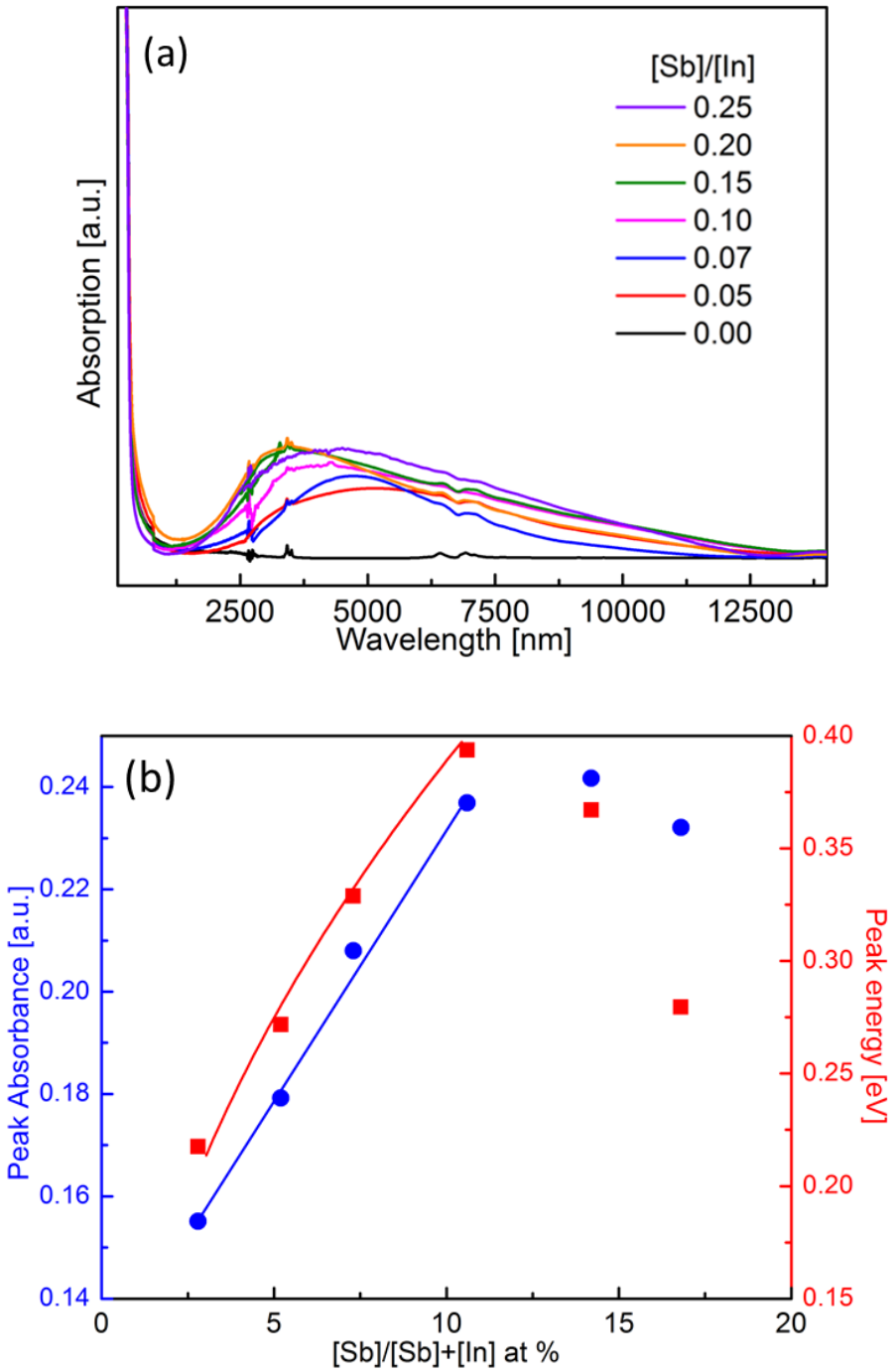

Figure 3.10: (a) Normalized absorption spectra of AIO NCs ranging from UV to MIR. Different doping concentration ratios ([Sb]/[In]) are indicated in the graph. (b) Maximum plasmon band absorbance (blue circles) and peak energy (red squares) as a function of Sb doping concentration, [Sb]/([Sb]+[In]).

As predicted from eq.1.1, the absorption intensity increases linearly with increasing Sb doping concentration, due to the corresponding increase in the free electron concentration (N). The dependence of plasmon band energy on the Sb doping concentration is shown in Figure 3.10 (b). The energy of plasmon band shifts to higher energy with increasing Sb concentration up to ca. 10.6 at %. Further increase in doping concentration leads to the trends shifting back to lower energy due to electron trapping around the Sb doping sites.[50] Peak energy positions are well fit to eq 1.2 for Sb doping concentrations below ca. 10.6 at. % (red line), indicating the square root dependence of the peak energy on the doping concentration. Based on the optical parameter values for bulk bcc-In_2O_3 ($m^*=0.3m_0$, $\varepsilon_{opt}=4.0$),[57] the maximum concentration of free electrons in AIO NCs is determined to be ca. 1.24×10^{20} cm^{-3} (for 10.6 at % of Sb). The feature of both plasmon energy and intensity matches very well with the Drude model for the free electron gas formation in semiconductors.[17]

3.5 Further Elucidation of Electronic and Optical Properties of AIO NCs by Simulation

In order to understand the origin of electronic and optical properties of AIO NCs quantitatively, the electronic structure calculations were performed within the DFT formalism, using Quantum Espresso package with the plane-wave basis set for valence electronic

configuration and pseudopotential for the electron-ion interactions. In addition, the exchange-correlation potential was implemented in the GGA using PBE functional.

The supercell of In_2O_3 was constructed consisting of 80 atoms, with a lattice parameter of 10.137 Å. The valence electron configurations for elements are shown as follows: Sb-$5s^2 5p^3$, In-$5s^2 5p^1 4d^{10}$ and O-$2s^2 2p^4$. As the b-sites of indium were found to be more energetically favorable for substitution, two of the b-sites were replaced by Sb atoms, representing a doping ratio of 6.25%.[58] After geometrical optimization, the criteria of total energy for the fully relaxed structure was converged to less than 10^{-4} eV and total force less than 0.01 eV/Å on each atom (2×2×2 k-point mesh). For self-consistent field (SCF) calculations, the k-point sampling of the Brillouin zone was constructed using Monkhorst-Pack scheme with 3×3×3 grids in the supercell of In_2O_3 with a cut-off energy 500 eV. The energy was converged to 10^{-6} eV after 12 itinerary cycles. For non self-consistent field (NSCF) calculations, a much denser grid of 6×6×6 was used with 500 eV cut-off energy to get more accurate controlling of the calculated results.

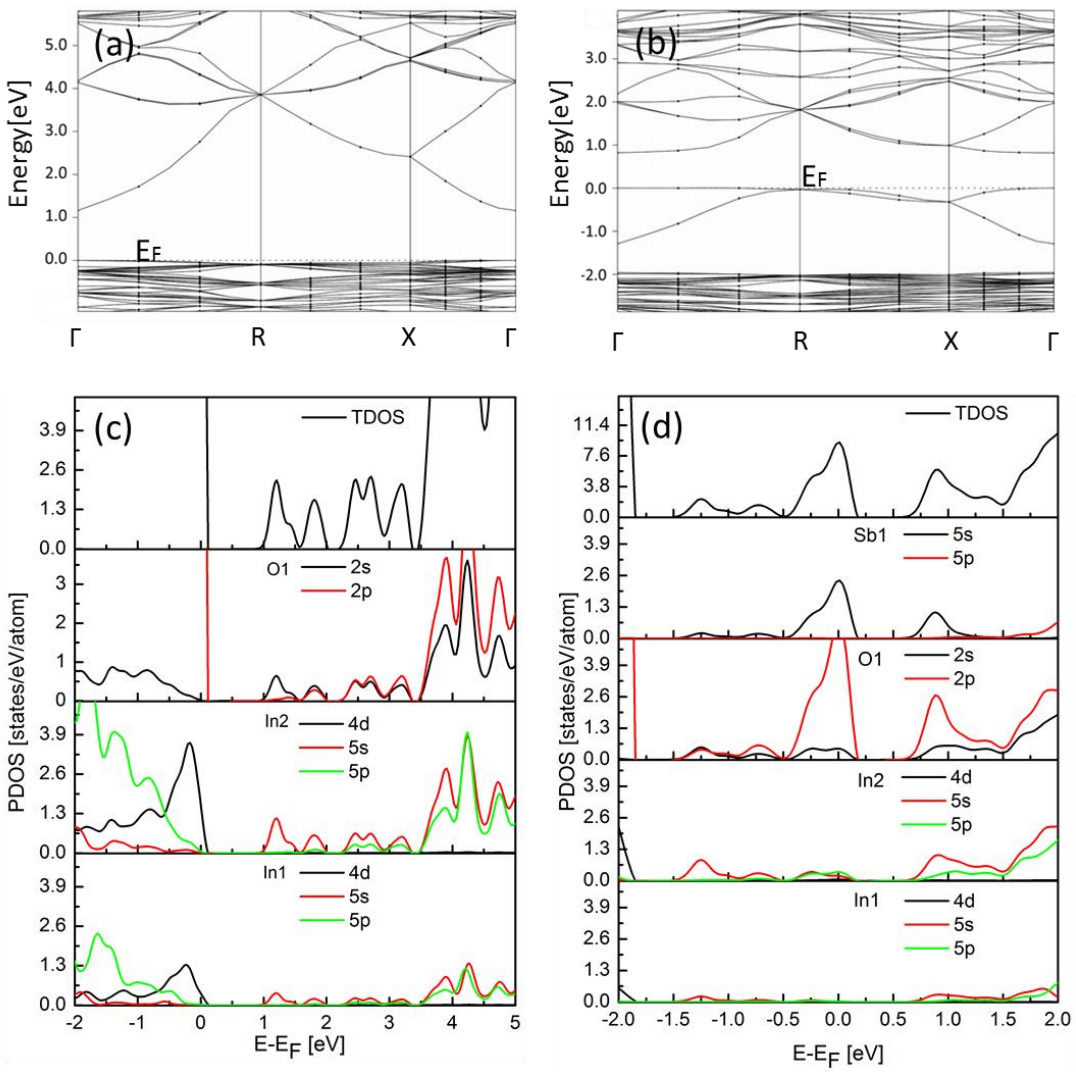

Figure 3.11: Calculated band structures (top) and densities of states (bottom) of pure and Sb-doped In_2O_3. E_F is set at 0 eV. TDOS denotes total density of states. The units of partial density of states are states eV^{-1} $atom^{-1}$. In1 and In2 correspond to b-site and d-site of In, respectively.

After geometrical optimization of structures, the electronic band structures and DOS of the pure and Sb-doped In_2O_3 were calculated and are shown in the Figure 3.11. As shown in the band structure of In_2O_3 in Figure 3.11 (a), both the bottom of the conduction band and the top of the valence band are located in the same Γ point of the Brillouin zone, which indicates that In_2O_3 is a direct-band-gap semiconductor. The calculated band gap, 1.2 eV is much smaller than the

experimental value, owing to the well-known underestimation of the band gap by DFT.[43] The parabolic bottom of the conduction band is mainly contributed by the 5s states of indium and partially O 2p as indicated in the PDOS of In_2O_3 in Figure 3.12 (b). It is observed that the conduction band of Sb-doped In_2O_3 is significantly altered, compared with that of pure In_2O_3. Sb doping causes the shift of the Fermi level up and above the conduction band minimum. The bottom of the conduction band is of dominant In 5s and partial Sb 5s orbitals but with strong hybridization with O 2p states. In addition, the dopant electronic states at the top of the band around 0 eV are localized near the Fermi level to some extent , which are detrimental to the electronic properties.[59]

3.6 Influence of Fast Annealing on the Performance of Plasmonic Properties of AIO NCs

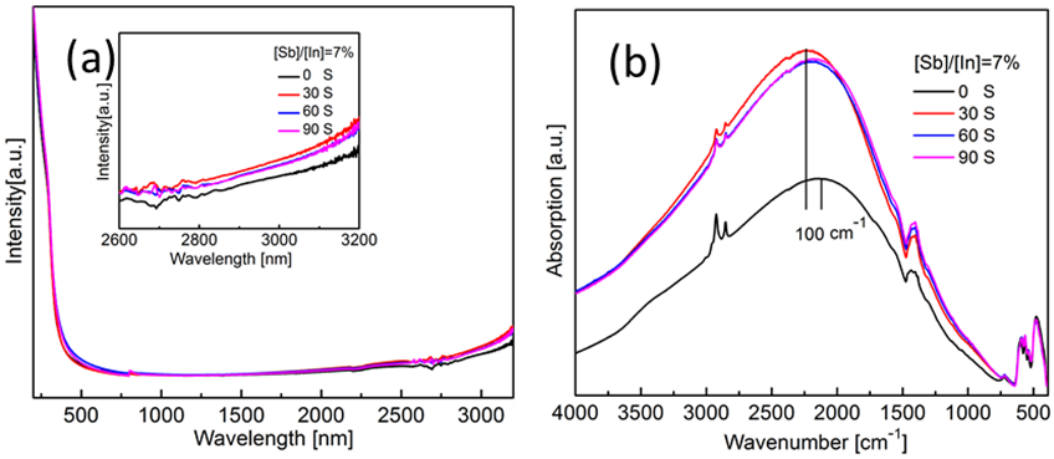

Figure 3.12: (a) UV-Vis-NIR absorption spectra and (b) FTIR absorption spectra of 7% AIO annealed under H_2 at 400 ºC for various times. Colloidal solution of AIO NCs was drop-casted on the quartz (UV-Vis-NIR) and KBr pellet (FTIR), respectively.

It is well known that heat and oxygen can influence plasmon properties of doped NCs greatly due to the change of the surface or point defect electronic structure. In the case of 7% AIO NCs, fast annealing under H_2 was conducted on the AIO NCs deposited on the substrate. It is evident that the plasmon intensity is enhanced dramatically and maximized for absorption in both NIR edge and MIR range with 30 s fast heating, together with 100 cm^{-1} blue-shift to higher energy. Surprisingly, the further heating decreases the intensity of the peak for both spectra. It is proposed that fast annealing can activate the dormant dopant and then donate more free electrons. However, further heating may lead to the formation of dopant oxides, resulting in the decrease of the absorption intensity. Similar post-synthesis treatment of annealing was carried out for 7% AIO NCs under the Ar atmosphere. As shown in Figure A5 (a), intensity of the plasmon can be enhanced with the similar effect as H_2 but without further shift of the peak position. Furthermore, Figure A5 (b) indicates that annealing under H_2 at 400 ^{o}C enable the recovery of the plasmon for the oxidized 7% AIO NCs. Hence, it is confirmed that annealing under different atmosphere is one effective method to adjust the plasmon band of the AIO NCs.

3.7 Conclusion

Antimony-doped In_2O_3 NCs have been successfully synthesized in colloidal solution, showing the well-tuned plasmonic property based on the doping precursor ratio of the [Sb]/[In] of the NCs.

Structure characterization of XRD shows that secondary metallic Sb can emerge for AIO NCs with high doping ratio of [Sb]/[In], like 0.20 and 0.25, probably due to the disproportionation of Sb^{3+} or reductive environment of solvent oleylamine. TEM imaging reveals that relatively

uniform AIO NCs are formed with lower doping ratio while nanoflowers of AIO NCs are achieved at high doping ratio. This distinct morphology of AIO NCs can be ascribed to the role of Cl^-, weakening the protection of oleylamine and contributing to the assembly of the AIO NCs. Besides, high doping ratio of [Sb]/[In] leads to a strong distortion of the AIO NC as evidenced by the Raman spectra.

Spectroscopy was employed to gain more information about the electronic and optical properties. Both UV-Vis-NIR absorption spectra and FTIR absorption spectra were carefully combined, based on the overlapping part near the edge of NIR to study the plasmonic behavior of the AIO NCs. It is revealed that the plasmon of doped AIO NCs can be well-tuned from 0.25 eV to 0.37 eV in the MIR with the maximum doping concentration of Sb, ca. 10.6 %. Accordingly, the highest concentration of free electrons in AIO NCs is determined to be ca. 1.24×10^{20} cm^{-3} (for 10.6 %). In addition, UV-visible spectra confirmed a blue shift of the band gap of AIO NCs, due to the Burstein-Moss effect. Aside from the doping-dependant tuning of the plasmon, intensity of the plasmon band of AIO NCs can be also improved noticeably using fast annealing at 400 ºC under reductive H_2 gas atmosphere.

Chapter 4 Studies of Structures and Optical Properties in Titanium-doped Indium Oxide Nanocrystals

4.1 Crystal Structure and Morphology of TIO NCs

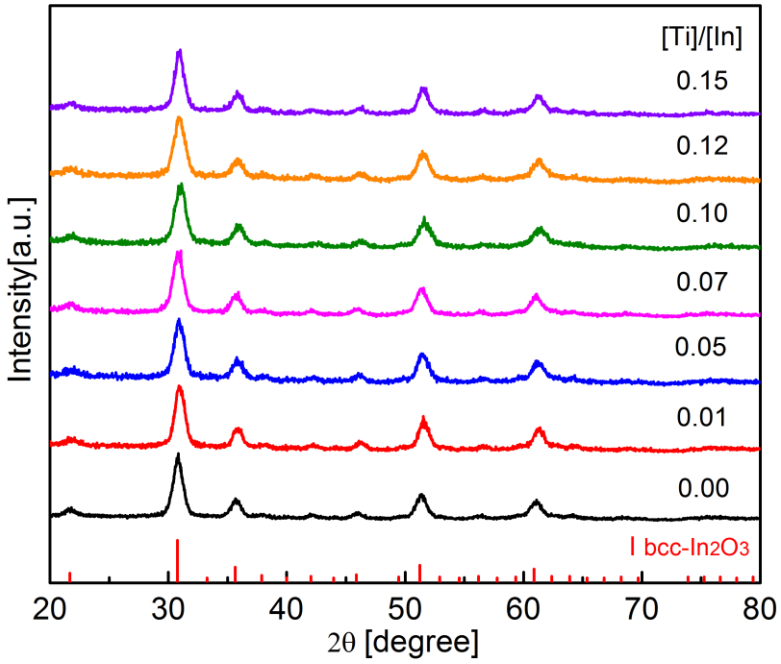

Figure 4.1: XRD patterns of Ti-doped In_2O_3 NCs, synthesized at 250 °C with different starting Ti concentrations indicated in the graph. Red lines at the bottom correspond to the XRD pattern of bulk bcc-In_2O_3 (JCPDS 06-0416).

Figure 4.1 shows the XRD patterns of the TIO NCs with various doping concentrations, as indicated in the graph. It is evident that all patterns of the TIO NCs are in very good agreement with bulk bcc-In_2O_3 reference pattern. The average particle size, obtained from Scherrer equation, is ca. 8.5 nm.

Figure 4.2 displays overview TEM images and corresponding HRTEM images of TIO NCs. It is observed that the sizes of both 1% TIO and 10% TIO NCs seem to be distributed randomly for both samples in overview image (a) and (c), respectively. Notably, HRTEM images in (b) and (d) illustrate the clear lattice fringes of AIO NCs, confirming the single crystalline nature of the NCs. Additionally, the measured lattice spacings indicated in HRTEM images correspond to the crystal planes of bulk bcc-In_2O_3.

Furthermore, quasi-spherical shapes of TIO NCs are observed in the HRTEM images. Unlike the Sb-doped In_2O_3 NCs, no nanoflower-like NCs were present in the HRTEM image. It is speculated that the titanium isopropoxide forms the gel-like network, which contributes to the faceted TIO NCs and prevents the assembly of TIO NCs into nanoflower even at higher doping ratio.

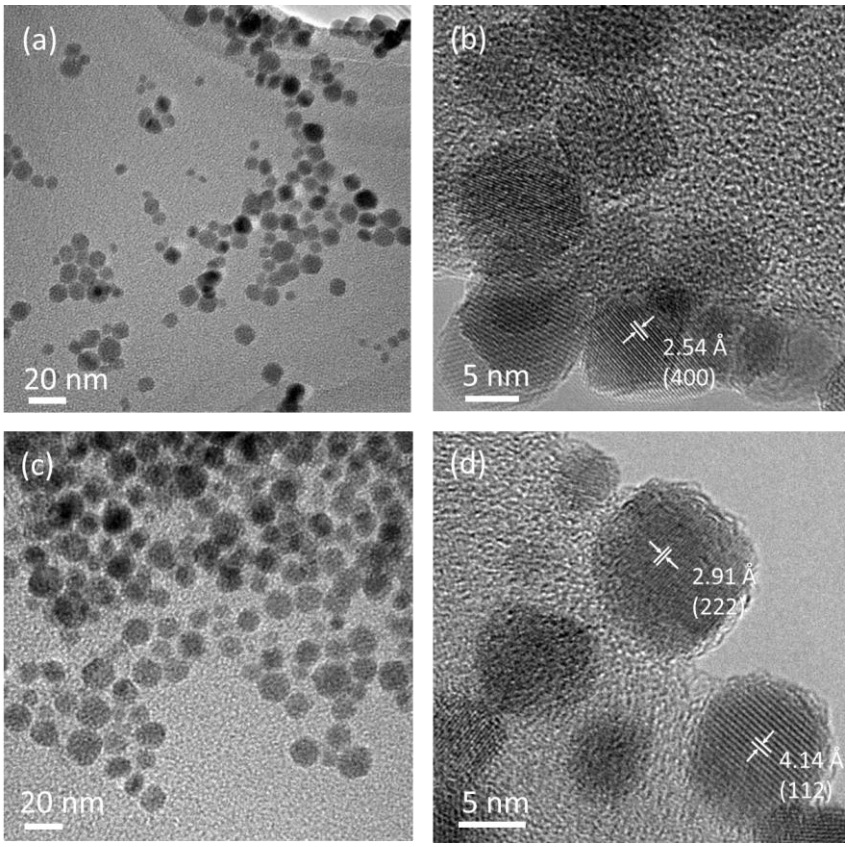

Figure 4.2: Representative overview TEM image of TIO NCs with starting [Ti]/[In] of 1% (a) and 10% (c), respectively. Corresponding HRTEM images of quasi-spherical TIO NCs are shown in image (b) and (d).

4.2 Elemental Analysis of TIO NCs

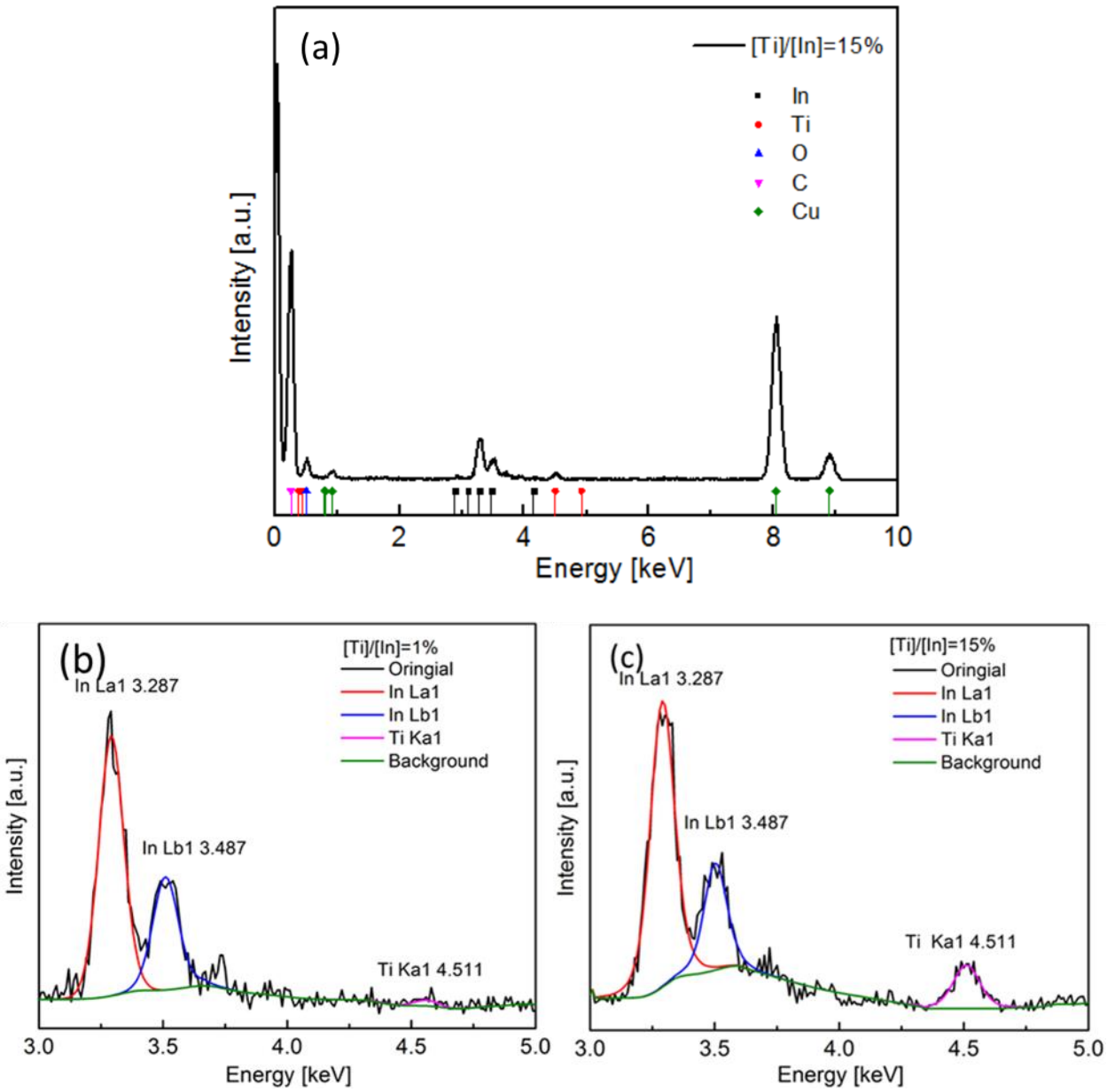

Figure 4.3: EDX spectrum of representative 15% TIO NCs (a) together with enlarged spectrum of 1% TIO NCs (b) and 15% TIO NCs (c), respectively. Lines at the bottom of Figure (a) correspond to the photon energy of characteristic X-ray for different elements.

Figure 4.3 (a) presents the EDX spectrum of 15% TIO NCs, containing the peaks for In, Ti, O, C and Cu. A remarkable difference of Ti Kα peak intensity can be observed between 1% TIO NCs (Figure 4.3 (b)) and 10% TIO NCs (Figure 4.3 (c)). The obtained actual doping content of Ti in colloidal TIO NCs as determined by EDX spectra is listed in Table 4.1.

Table 4.1: Actual doping content of Ti in colloidal TIO NCs as determined by EDX spectra

Starting Ti content ([Ti]/[In] at. %)	Ti content in TIO NCs (at. %)
1	1.1
5	3.7
7	6.1
10	8.5
12	10.3
15	12.4

Except for 1 % TIO NCs, the actual doping content of Ti in AIO NCs is overall lower than that of the starting [Ti]/[In]. From the kinetic perspective on doping mechanism, the relatively lower reactivity of the Ti precursor is likely to hinder the incorporation of dopants into the nucleated NCs, owing to its slower binding rate than the host indium cations.

Furthermore, XPS spectroscopy was also employed to determine the concentration as well as the oxidation state of dopant, Ti.

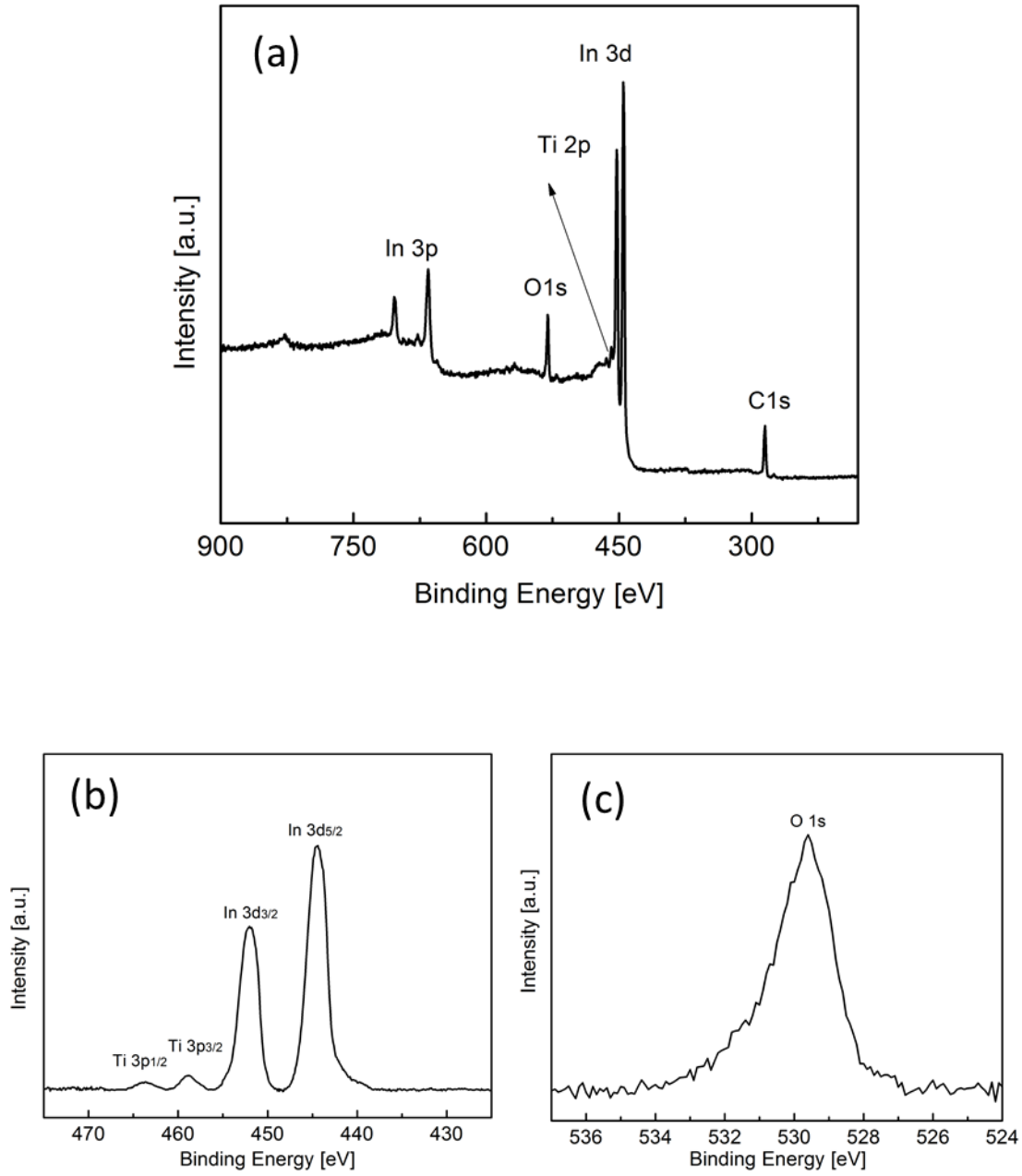

Figure 4.4: (a) Representative XPS survey spectrum of 10 % TIO NCs. (b) High-resolution XPS spectrum of In 3d region and Ti 3p regions. (c) High-resolution XPS spectrum of O1s region.

The survey spectra obtained for 10% TIO NCs in Figure 4.4 (a) demonstrate the existence of elements, including carbon, oxygen, indium and titanium.

High-resolution XPS spectrum of In 3d region and Ti 3p region is shown in Figure 4.4 (b). In terms of the In 3d peaks, the determined binding energies are 452.4 eV for In $3d_{3/2}$ and 444.9 eV for In $3d_{5/2}$.[60] The doublet peaks of Ti $2p_{1/2}$ and Ti $2p_{3/2}$ are situated at ca. 463.6 and 458.9 eV, respectively.[60]

The total Ti content determined for the representative 10% TIO NCs by XPS is 8.4%, which is similar to the value obtained by EDX, as depicted in Table 4.1. In addition, the EDX elemental maps obtained in STEM modes (Figure B1) shows all elements, including Ti, In, and O, evenly distributed across selected area of 10% TIO NCs. This indicates that the dopant, Ti is homogeneously distributed throughout the TIO NCs.

4.3 Spectroscopic Studies of TIO NCs

4.3.1 Raman Spectra of TIO NCs

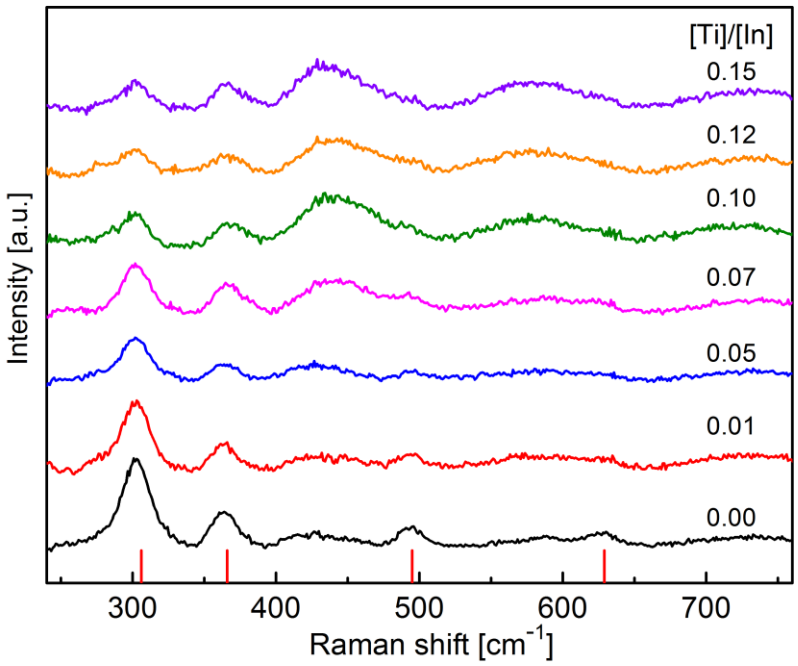

Figure 4.5: Raman spectra of TIO NCs with different starting Ti doping concentrations indicated in the graph. Red lines at the bottom correspond to the Raman peaks of bulk bcc-In_2O_3.

To gain more insight into the crystal structure of the TIO NCs, Raman spectra were recorded for TIO NCs with different doping concentrations and shown in Figure 4.5. In contrast with the characteristic of Raman modes for undoped In_2O_3 NCs, continuous weakening and broadening of the characteristic peaks are observed for TIO NCs with increasing doping concentration. In particular, weak Raman peaks at low frequencies, 307 and 366 cm^{-1} disappeared eventually for TIO NCs with doping ratio of [Ti]/[In] above 0.07, implying the local distortion of the local crystal lattice despite the consistent XRD patterns of TIO NCs with pure In_2O_3 NCs.

4.3.2 UV-Vis-NIR Absorption Spectra of TIO NCs

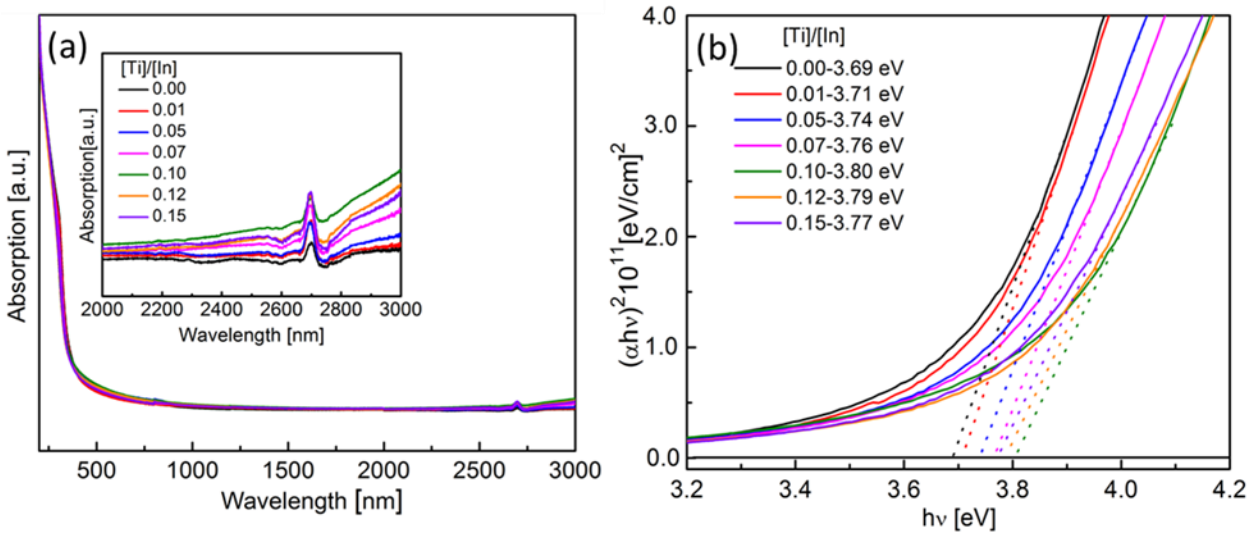

Figure 4.6: (a) Band-gap-normalized UV-Vis-NIR absorption spectra of TIO NCs with measured wavelength from 200 nm to 3000 nm. Inset is enlarged absorption spectra in NIR region with indicated different starting doping concentration ([Ti]/[In]) inside. (b)Tauc plot of optical band gap shift of TIO NCs with indicated various doping concentrations and corresponding band gap values.

Figure 4.6 (a) illustrates the band-gap-normalized UV-Vis-NIR absorption spectra with different doping concentrations ([Ti]/[In]) as shown in the graph.The absorption intensities of TIO NCs in the NIR region increase gradually with the increase in doping ratio, up to 10% , implying the increased concentration of electrons introduced by doping of Ti. Further increase in doping ratio leads to the opposite trend of the intensity, due to the electron trap states around the dopant Ti.

Furthermore, increased concentration of electrons introduced by doping of Ti also contributes to the increase in optical band gaps of TIO NCs, owing to the Burstein-Moss effect.

Both increased absorption edge in NIR and band gap shift of TIO NCs with various doping concentrations suggest the signature of the plasmon in the doped semiconductor NCs.

4.3.3 FTIR Absorption Spectra of TIO NCs

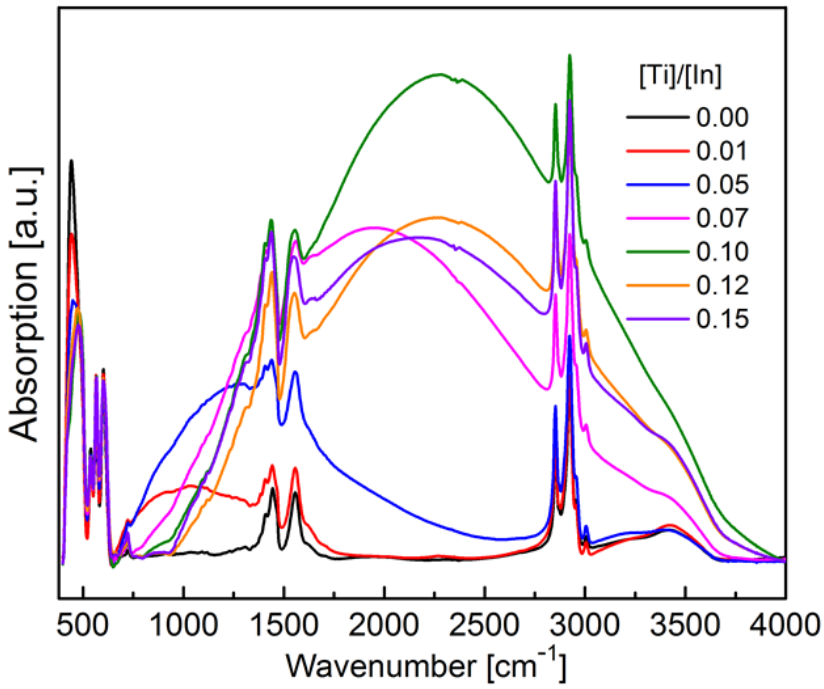

Figure 4.7: Normalized FTIR absorption spectra of TIO NCs with different doping concentrations indicated in the graph.

Given the weak absorption edge of TIO NCs in the NIR range, all FTIR absorption spectra of TIO NCs with different doping concentrations were normalized based on peak intensity of the phonon vibration, located at 564 cm^{-1} for the quantitative analysis of the absorption of plasmon versus doping concentration.

4.4 Analysis of the Plasmonic Properties of TIO NCs by Drude Model

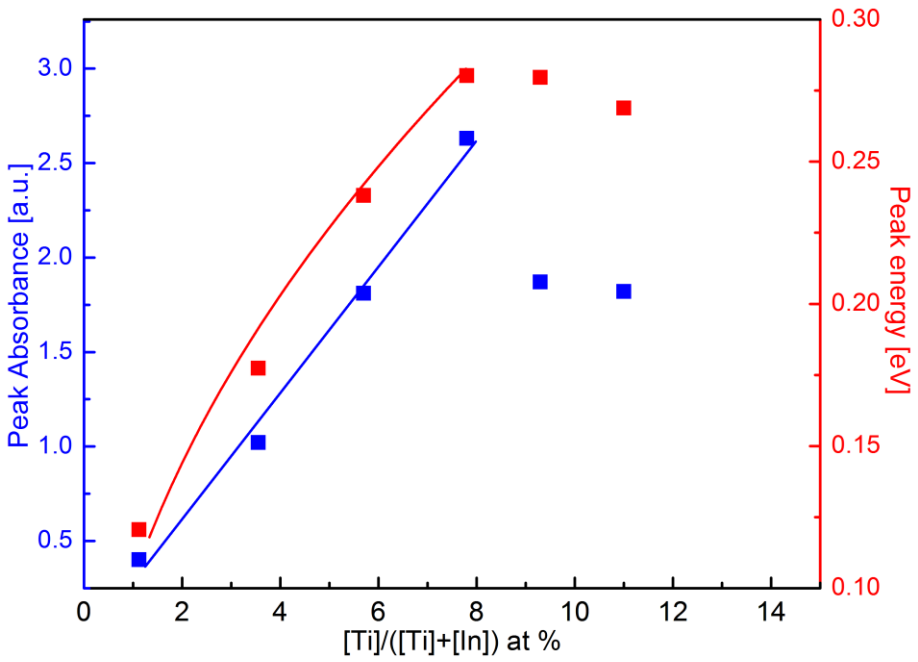

Figure 4.8: Maximum plasmon band absorbance (blue squares) and peak energy position (red squares) as a function of Ti doping concentration, [Ti]/([Ti]+[In]).

The correlation between plasmonic properties and doping concentration of TIO NCs are shown in Figure 4.8. The absorption intensity increases linearly with increasing Ti doping concentration as expected from eq.1.1, due to the corresponding increase in the free electron concentration (N). Accordingly, plasmon band of TIO NCs shifts to higher energy with increasing doping concentration of Ti up to ca. 7.8 at %. Further increase in doping concentration causes the reverse shift of the plasmonic peak due to electron trapping around the Ti dopant. Based on the optical parameter values for bulk bcc-In_2O_3 ($m^*=0.3m_0$, $\varepsilon_{opt}=4.0$), the maximum concentration of free electrons in TIO NCs is determined to be ca. 6.85×10^{19} cm^{-3} (for 7.8 at % of Ti). Well-matched fitting of both plasmon energy and intensity versus doping concentration to the Drude model indicate the free electron gas formation in semiconductor NCs.

4.5 Further Elucidation of Electronic and Optical Properties of TIO NCs by Simulation

For calculations of TIO NCs, similar simulation method and computational details are used as described in section 3.5. In the case of TIO, Ti $3s^2 3p^6 3d^2 4s^2 4p^0$ was referred to as valence electron configuration. In particular, the same doping ratio, 6.25% was applied in the case of TIO simulation. Ultrasoft pseudopotential was employed to describe the interaction of ion and electron, accompanied by the exchange-correlation component of PBE in GGA.

Calculated band structures and densities of states for TIO NCs are presented in Figures 4.9. In Figure 4.9 (a), the Fermi energy level of TIO shifts up much more in the band structure, along with the strong dispersion of the CB, compared with that of AIO. From the theoretical perspective, the Fermi energy value of TIO should lead to higher concentration of electrons and blue shift of the plasmon band, which is contrary to the experimentally observed results for AIO and TIO NCs. We propose that more trap states are formed in TIO NCs during the synthesis, resulting in the lower free electron concentration and red shift of the plasmon band. In addition, much smaller band gap is determined for TIO, which is attributed to the underestimation of the band gap calculation in DFT. In Figure 4.9 (b), the partial densities of states indicate that the valence states are mainly composed of the O 2p and In 5s states, while the conduction band states are made of the In 5s, O 2p, and Ti 3d. The overlap between orbitals of the cations and the anions around the Fermi energy level provides a transport network for charge carriers. [59]

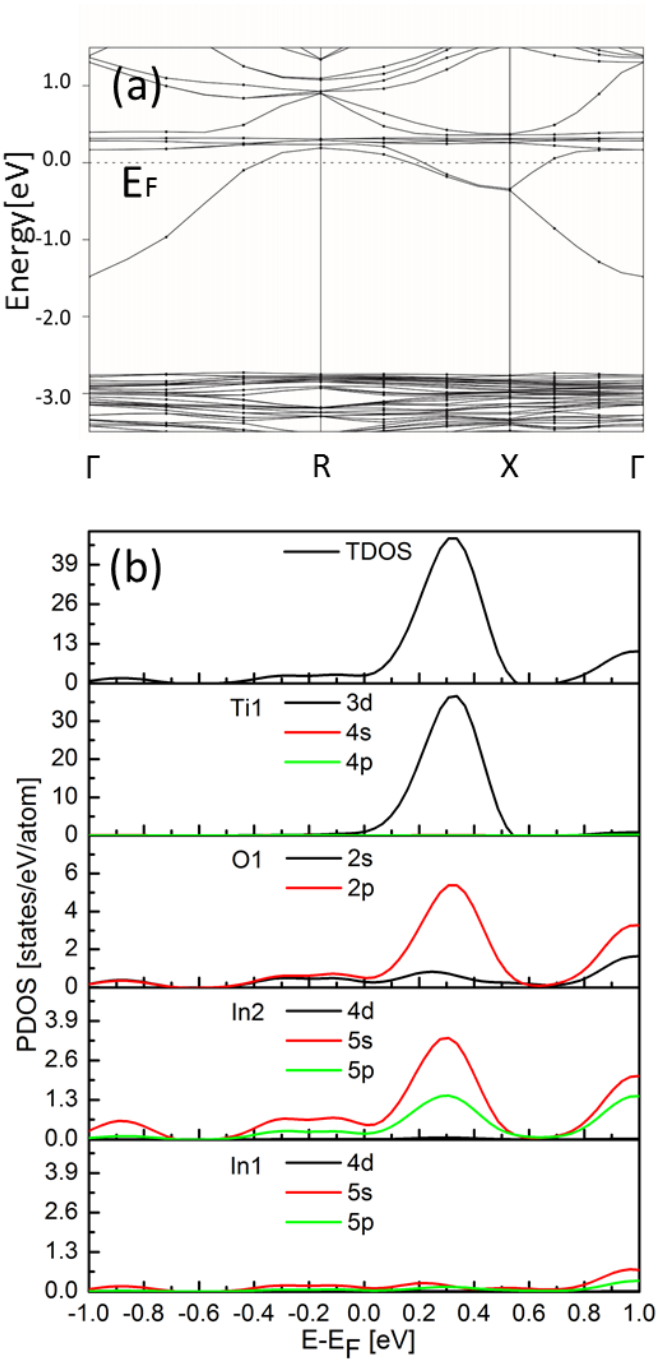

Figure 4.9: Calculated band structures (a) and densities of states (b) of Ti-doped In_2O_3. E_F is set at 0 eV. TDOS denotes total density of states. The units of partial density of states are states eV^{-1} $atom^{-1}$. In1 and In2 correspond to b-site and d-site of In, respectively.

4.6.Influence of the Size on the Plasmonic Behavior of TIO NCs.

In order to explore the influence of the size on the plasmonic behavior of TIO NCs, 10% Ti-doped In_2O_3 was chosen as a model system. A series of samples were synthesized at different temperatures, from 230 ºC to 300 ºC with reaction kept at the desired temperature for one hour. Figure 4.10 shows that all patterns of 10% TIO NCs agree very well with that of bulk bcc-In_2O_3.

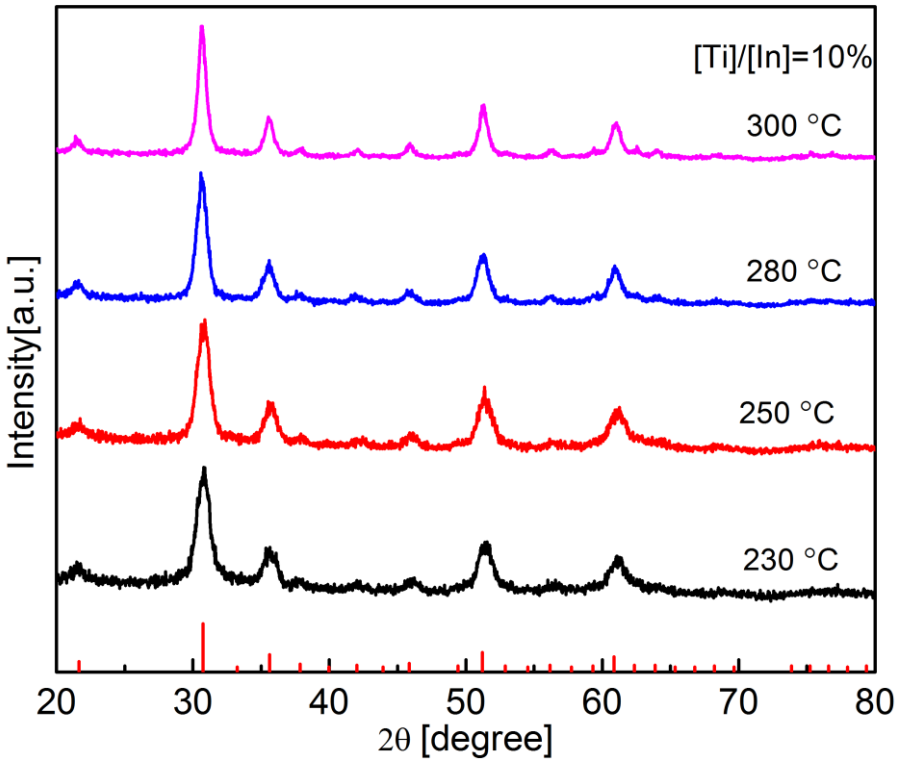

Figure 4.10: XRD Patterns of 10% TIO NCs synthesized at different temperatures. Red lines (bottom) correspond to the XRD pattern of bulk bcc-In_2O_3.

Table 4.2: Parameters extracted from XRD patterns of 10% TIO NCs synthesized at different temperatures

T [°C]	Particle Size [nm]	2θ of the (222) Reflection
230	7.77	30.79
250	8.16	30.98
280	8.49	30.91
300	12.48	30.92

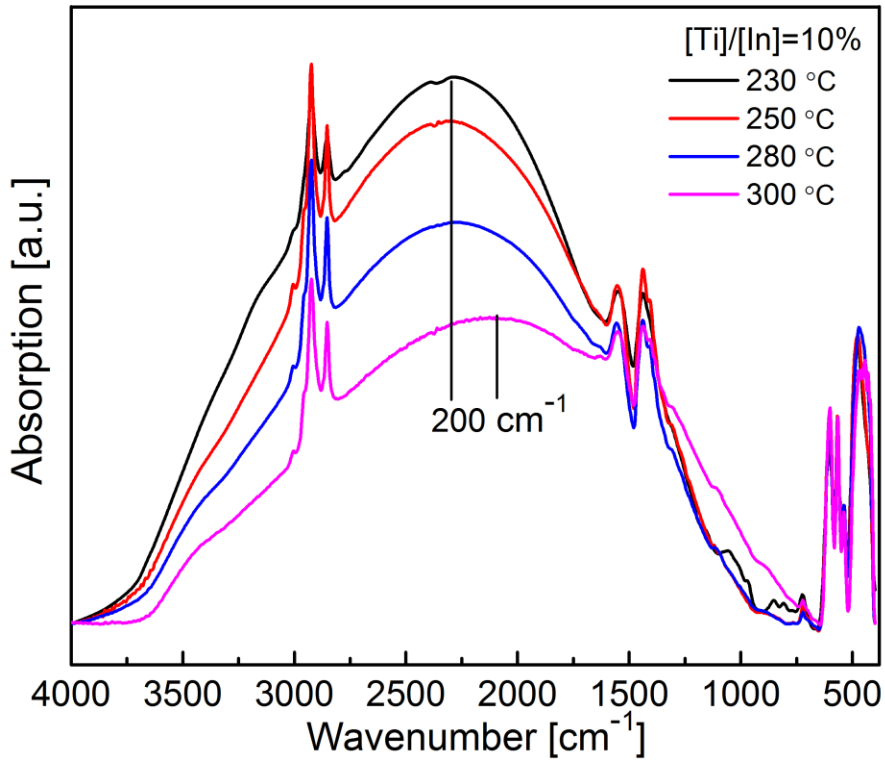

Figure 4.11: FTIR spectra of 10% TIO NCs synthesized at different temperatures.

To gain further insight into the relationship between NC size and synthesis temperature, the particle sizes of samples synthesized at different temperatures were calculated by the Scherrer equation (eq 2.1). Table 4.3 shows the summaries of the particle sizes obtained by the Scherrer equation and 2θ values, corresponding to the bcc-In_2O_3 (222) diffraction. It is apparent that the increase in reaction temperature gives rise to the large size of Ti-In_2O_3 NCs since the high temperature accelerates the growth of NCs. It is consistent with the relatively narrow main peak (222) around ca.31 degrees at high temperature as shown in Figure 4.10.

In Figure 4.11, it is obvious that the intensity of the 10% TIO NCs drops gradually with increasing synthesis temperature. In particular, the plasmon peaks for sample synthesized at 300 ^{o} C shifts to shorter wavenumber, indicating higher possibility of precursor dopants expelled from the doped NCs at high temperature.

4.7 Effect of Fast Annealing on the Performance of Plasmon of TIO NCs

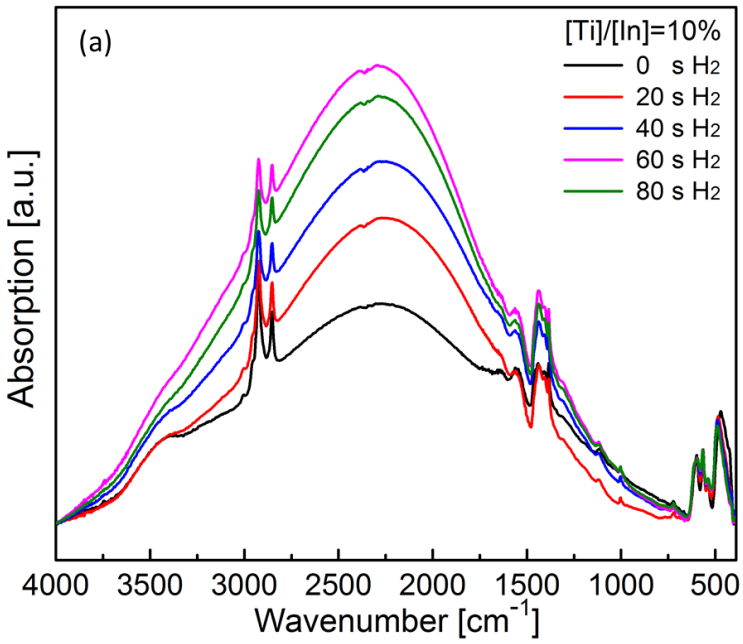

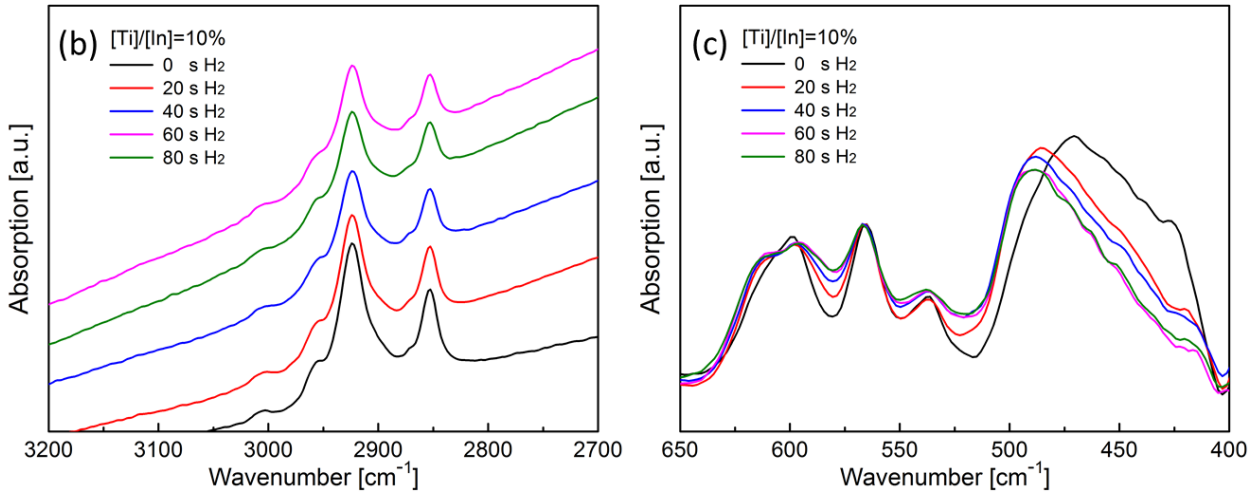

Figure 4.12: (a) FTIR spectra of 10% TIO NCs annealed under H_2 at 400 ºC with different duration of time. (b) Enlarged spectra of two sharp peaks from CH_2 stretch. (c) Enlarged spectra of phonon vibrations of In-O.

Table 4.3: Q factors of 10% TIO NCs annealed under H_2 with different duration of time.

Time/s	Q factors
0	1.34
20	1.54
40	1.55
60	1.57
80	1.56

It is observed that the absorption intensities of 10% TIO NCs increase dramatically with fast annealing under H_2 at 400 ^{o}C from 20 s to 60 s, without any peak shift of the plasmon. Based on the eq 1.1 and 1.2, this specific phenomenon can be attributed to the decreased mean free time, τ, indicating the alteration of the crystallinity for TIO NCs. Furthermore, no band gap shift is

observed in the UV-Vis absorption spectra of 10% TIO annealed under H_2 at 400 °C for various times, excluding the change in the free carrier concentration. Moreover, fast annealing also contributes to the decreased intensity of two sharp peaks from CH_2 stretch. In addition, after annealing, there is not any deviation of the normalized peak, around 564 cm^{-1}, which supports the assumption of normalization based on this steady phonon vibration, mentioned in section 3.3.3.

In addition, Q factors were calculated based on the ratio of the energy of the peak to the FWHM to evaluate the quality of these plasmon peaks.[61] Table 4.3 represents all Q factors of 10% TIO NCs annealed under H_2 with different duration of time. Similar to the maximized intensity achieved by the sample annealed for the 60 s, the highest Q factor value belongs to the same sample.

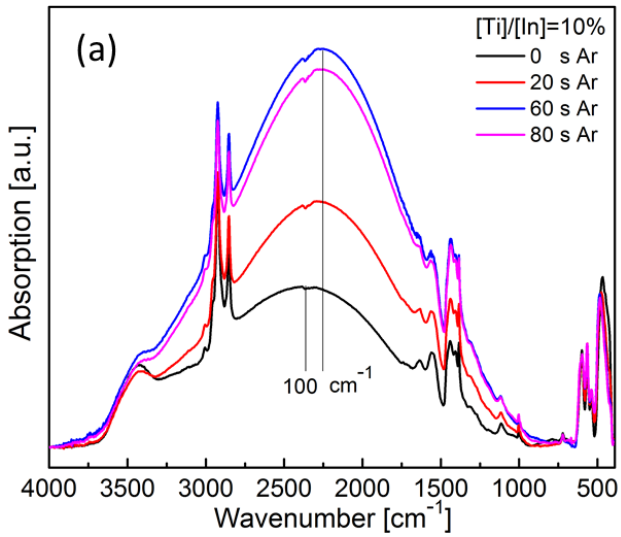

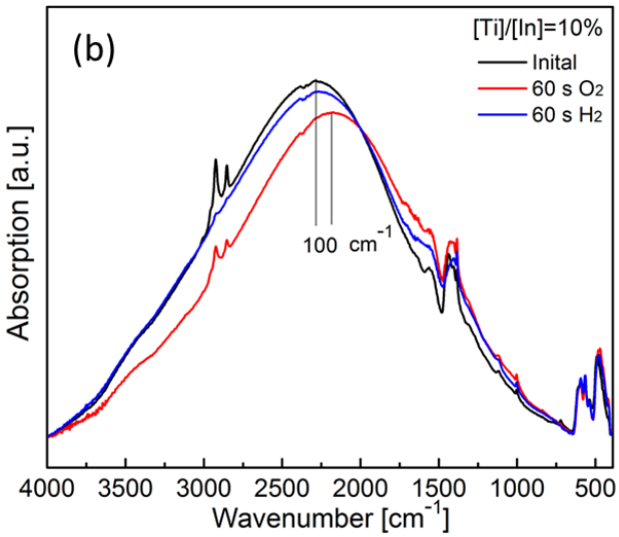

Figure 4.13: FTIR spectra of 10% TIO NCs annealed under Ar with different duration of time (a) and recovery of FTIR spectra for oxidized 10% TIO NCs by H_2 reduction (b).

Similar post-synthesis treatment by thermal annealing was carried out under the Ar atmosphere. Figure 4.13 (a) clearly demonstrates that intensity of the plasmon can be enhanced with the same effect as H_2. However, a red-shit of 100 cm^{-1} is also observed for all annealed samples under Ar, which might be attributed to trapping of electrons, due to the trace of O_2 adsorbed on the surface of NCs.[62] Furthermore, Figure 4.13 (b) reveals that annealing under H_2 at 400 ºC allows for the regeneration of the plasmon for the oxidized 10% TIO NCs.

Here, one conclusion can be drawn that fast annealing of TIO NCs under H_2 reduction within one minute can enhance the quality of the plasmon peak effectively, without any peak shifting.

4.8 Conclusion

Titanium-doped In_2O_3 NCs have been synthesized in colloidal solution, exhibiting the well-controlled plasmon based on the doping concentration of the NCs.

Both XRD patterns and TEM images were used for the fundamental characterization of crystal structure, indicating that all synthesized TIO NCs with different doping concentrations retain the bcc-In_2O_3 structure. Different from the nanoflowers of AIO NCs with higher doping concentration, faceted TIO NCs are observed for all doped samples in the HRTRM images, owing to the gel-like network from the titanium precursor during the synthesis.

Plasmon of TIO NCs in the MIR region can be tuned from 0.13 eV to 0.28 eV by varying the doping concentration of Ti from 1.12 % to 7.8 %. The highest concentration of free electrons determined for TIO NCs (7.8 %) is ca. 6.85×10^{19} cm^{-3}, relatively two times smaller than that for AIO NCs (NCs) with ca. 1.24×10^{20} cm^{-3}. Unlike the much broad plasmon peak of AIO NCs, covering both NIR and MIR, plasmon of TIO shows a relatively narrow peak in the MIR, which can be attributed to the less distorted crystal structure, confirmed by Raman spectra. Compared to AIO NCs, similar band gap shift was also observed in TIO NCs. Furthermore, simulation of TIO illustrates the n-type feature of the band structure. In addition, the electronic structures of the host lattice and dopant Ti were revealed by PDOS calculation, indicating the strong hybridization of the orbitals of the In 5s, O 2p, and Ti 3d for conduction band. Furthermore, in comparison with AIO, the calculated high Fermi energy level of TIO should theoretically correspond to the high electron concentration, which is contradictory with the experimentally observed results. It is suggested that the actual electron concentration of doped NCs can be also affected by some other factors, such as the surface trap states and defects.

The influence of the size on the plasmon of TIO NCs was also explored, illustrating that the plasmon of as-synthesized TIO NCs with various sizes is relatively unchanged, distinct from the size-dependent plasmon of the noble metal NCs, such as gold and silver NCs. In addition, the quality of the plasmon band of TIO NCs can be improved appreciably with higher Q factor, using fast annealing under H_2.

Future Perspective

Although doped In_2O_3 NCs have illustrated well-tuned plasmon based on the composition, some further experiments and analyses have yet to be completed. Regarding AIO NCs, controlling the ratio of Sb^{5+} to Sb^{3+} is a crucial step for the further manipulating the plasmonic behavior of AIOs. One proposed method is to conduct the reactions with different starting concentration ratio of $[Sb^{5+}]/[Sb^{3+}]$. Besides, new dopant precursor, like $Sb(acac)_3$ can be utilized to get more crystalline NCs and optimize the broad plasmon band without the effect of the Cl^- on the AIO NCs.

With respect to TIO NCs, the effect of the titanium precursor, as well as the Cl^- ions on the shape of TIO NCs is worthwhile exploring, since plasmon could be also possibly tuned by the shape of the semiconductors. Besides, the other doping method, like hot-injection can be used to improve the doping efficiency of titanium and, therefore, to expand the tuning range of the plasmon.

Lastly, as-synthesized NCs are expected to be exploited as building blocks for other composite and sensing material for special needs. In addition to completion of studies with AIO and TIO NCs for plasmon, the strategy of codoping can be utilized to combine different optical, electronic, or magnetic properties together. For instance, Co and Ti codoped In_2O_3 NCs could be an interesting model system for exploring the interaction of magnetic and plasmonic properties simultaneously.

References

1. Greiner, R. A., *Semiconductor Devices and Applications;* McGraw-Hill Book Company : New York, 1961.

2. West, A. R., *Basic Solid State Chemistry*, 2nd Ed.; John Wiley and Sons, Ltd.: Chichester, 1999.

3. Farvid, S. S.; Dave, N.; Radovanovic, P. V., *Chem. Mater.* **2009,** *22*, 9-11.

4. Robertson, J.; Gillen, R.; Clark, S. J., *Thin Solid Films* **2012,** *520*, 3714-3720.

5. Murali, A.; Barve, A.; Leppert, V. J.; Risbud, S. H.; Kennedy, I. M.; Lee, H. W., *Nano Lett.* **2001,** *1*, 287-289.

6. Hamberg, I.; Granqvist, C. G., *J. Appl. Phys.* **1986,** *60*, 123-160.

7. Zhuang, Z.; Peng, Q.; Liu, J.; Wang, X.; Li, Y., *Inorg. Chem.* **2007,** *46*, 5179-5187.

8. Farvid, S. S.; Hegde, M.; Radovanovic, P. V., *Chem. Mater.* **2013,** *25*, 233-244.

9. Layek, A.; Yildirim, B.; Ghodsi, V.; Hutfluss, L. N.; Hegde, M.; Wang, T.; Radovanovic, P. V., *Chem. Mater.* **2015,** *27*, 6030-6037.

10. Nadaud, N.; Lequeux, N.; Nanot, M.; Jove, J.; Roisnel, T., *J. Solid State Chem.* **1998,** *135*, 140-148.

11. Shannon, R., *Solid State Commun.* **1966,** *4*, 629-630.

12. Farvid, S. S.; Dave, N.; Wang, T.; Radovanovic, P. V., *J. Phys. Chem. C* **2009,** *113*, 15928-15933.

13. Farvid, S. S.; Radovanovic, P. V., *J. Am. Chem. Soc.* **2012,** *134*, 7015-7024.

14. Banfield, J., *J. Mater. Chem.* **1998,** *8*, 2073-2076.

15. Hutfluss, L. N.; Radovanovic, P. V., *J. Am. Chem. Soc.* **2015,** *137*, 1101-1108.

16. Mourdikoudis, S.; Liz-Marzán, L. M., *Chem. Mater.* **2013,** *25*, 1465-1476.

17. Wang, T.; Radovanovic, P. V., *J. Phys. Chem. C* **2010,** *115*, 406-413.

18. Lee, D. C.; Smith, D. K.; Heitsch, A. T.; Korgel, B. A., *Annual Reports Section" C" (Physical Chemistry)* **2007,** *103*, 351-402.

19. Dave, N.; Pautler, B.; Farvid, S.; Radovanovic, P., *Nanotechnology* **2010,** *21*, 134023-134029.

20. Mikulec, F. V.; Kuno, M.; Bennati, M.; Hall, D. A.; Griffin, R. G.; Bawendi, M. G., *J. Am. Chem. Soc.* **2000,** *122*, 2532-2540.

21. Erwin, S. C.; Zu, L.; Haftel, M. I.; Efros, A. L.; Kennedy, T. A.; Norris, D. J., *Nature* **2005,** *436*, 91-94.

22. Norris, D. J.; Efros, A. L.; Erwin, S. C., *Science* **2008,** *319*, 1776-1779.

23. Bryan, J. D.; Gamelin, D. R., *Prog. Inorg. Chem* **2005,** *54*, 47-126.

24. Dalpian, G. M.; Chelikowsky, J. R., *Phys. Rev. Lett.* **2006,** *96*, 226802.

25. In Kreibig, U.; Vollmer, M., *Theoretical Considerations in Optical Properties of Metal Clusters*; Springer,1995.

26. Kanehara, M.; Koike, H.; Yoshinaga, T.; Teranishi, T., *J. Am. Chem. Soc.* **2009,** *131*, 17736-17737.

27. McNay, G.; Eustace, D.; Smith, W. E.; Faulds, K.; Graham, D., *Appl. Spectrosc.* **2011,** *65*, 825-837.

28. Baba, A.; Aoki, N.; Shinbo, K.; Kato, K.; Kaneko, F., *ACS Appl. Mater. Interfaces.* **2011,** *3*, 2080-2084.

29. Faucheaux, J. A.; Stanton, A. L.; Jain, P. K., *J. Phys. Chem. Lett.* **2014,** *5*, 976-985.

30. Odom, T. W.; Nehl, C. L., *Acs Nano* **2008,** *2*, 612-616.

31. Franzen, S., *J. Phys. Chem. C* **2008,** *112*, 6027-6032.

32. Losego, M. D.; Efremenko, A. Y.; Rhodes, C. L.; Cerruti, M. G.; Franzen, S.; Maria, J.-P., *J. Appl. Phys.* **2009,** *106*.

33. Nütz, T.; Felde, U.; Haase, M., *J. Chem. Phys* **1999,** *110*, 110,12142-12150.

34. Wooten, F., *Optical properties of solids*. Academic Press: 2013.

35. Underwood, S.; Mulvaney, P., *Langmuir* **1994,** *10*, 3427-3430.

36. Chikan, V., *J. Phys. Chem. Lett.* **2011,** *2*, 2783-2789.

37. Nütz, T.; Felde, U.; Haase, M., *J. Chem. Phys* **1999,** *110*.

38. Stanley, R., *Nat. Photon.* **2012,** *6*, 409-411.

39. Li, D.; Ning, C., *Opt. Express* **2011,** *19*, 14594-14603.

40. Yao, Y.; Kats, M. A.; Genevet, P.; Yu, N.; Song, Y.; Kong, J.; Capasso, F., *Nano Lett.* **2013,** *13*, 1257-1264.

41. Milman, V.; Winkler, B.; White, J.; Pickard, C.; Payne, M.; Akhmatskaya, E.; Nobes, R., *Int. J. Quantum Chem.* **2000,** *77*, 895-910.

42. Giannozzi, P.; Baroni, S.; Bonini, N.; Calandra, M.; Car, R.; Cavazzoni, C.; Ceresoli, D.; Chiarotti, G. L.; Cococcioni, M.; Dabo, I., *J. Phys. Condens. Matter.* **2009,** *21*, 395502.

43. Pickett, W. E., *Computer Physics Reports* **1989,** *9*, 115-197.

44. Holzwarth, U.; Gibson, N., *Nat. Nanotechnol.* **2011,** *6*, 534-534.

45. Ferraro, J. R.; Nakamoto, K.; Brown, C. W., *Introductory Raman Spectroscopy*, 2nd ed; Elsevier, 2003.

46. Narayanaswamy, A.; Xu, H.; Pradhan, N.; Kim, M.; Peng, X., *J. Am. Chem. Soc.* **2006,** *128*, 10310-10319.

47. Du, N.; Zhang, H.; Chen, B.; Ma, X.; Liu, Z.; Wu, J.; Yang, D., *Adv. Mater.* **2007,** *19*, 1641-1645.

48. Wang, Y.; Brezesinski, T.; Antonietti, M.; Smarsly, B., *Acs Nano* **2009,** *3*, 1373-1378.

49. Wang, C. Y.; Dai, Y.; Pezoldt, J.; Lu, B.; Kups, T.; Cimalla, V.; Ambacher, O., *Cryst. Growth Des.* **2008,** *8*, 1257-1260.

50. Kim, S.-S.; Choi, S.-Y.; Park, C.-G.; Jin, H.-W., *Thin Solid Films* **1999,** *347*, 155-160.

51. Tanuševski, A.; Poelman, D., *Sol. Energ. Mat. Sol.* **2003,** *80*, 297-303.

52. Buonsanti, R.; Llordes, A.; Aloni, S.; Helms, B. A.; Milliron, D. J., *Nano Lett.* **2011,** *11*, 4706-4710.

53. Zhang, L.; He, R.; Gu, H.-C., *Appl Surf Sci* **2006,** *253*, 2611-2617.

54. Wu, N.; Fu, L.; Su, M.; Aslam, M.; Wong, K. C.; Dravid, V. P., *Nano Lett.* **2004,** *4*, 383-386.

55. Zhang, Y.; Li, J.; Li, Q.; Zhu, L.; Liu, X.; Zhong, X.; Meng, J.; Cao, X., *Scripta Mater* **2007,** *56*, 409-412.

56. Shim, M.; Guyot-Sionnest, P., *J. Am. Chem. Soc.* **2001,** *123*, 11651-11654.

57. Aliabad, H.; Hosseini, S.; Kompany, A.; Youssefi, A.; Kakhki, E. A., *Physica Status Solidi (b)* **2009,** *246*, 1072-1081.

58. Chen, Z.; Huang, L.; Zhang, Q.; Xi, Y.; Li, R.; Li, W.; Xu, G.; Cheng, H., *J. Phys. Chem. C* **2015,** *119*, 4789-4795.

59. Medvedeva, J. E.; Hettiarachchi, C. L., *Phys. Rev. B* **2010,** *81*, 125116-125132.

60. Marino, C. E.; Nascente, P. A.; Biaggio, S. R.; Rocha-Filho, R. C.; Bocchi, N., *Thin Solid Films* **2004,** *468*, 109-112.

61. Lounis, S. D.; Runnerstrom, E. L.; Bergerud, A.; Nordlund, D.; Milliron, D. J., *J. Am. Chem. Soc.* **2014,** *136*, 7110-7116.

62. Kramer, N. J.; Schramke, K. S.; Kortshagen, U. R., *Nano Lett.* **2015,** *15*, 5597-5603.

Appendix A: Antimony-doped Indium Oxide Nanocrystals

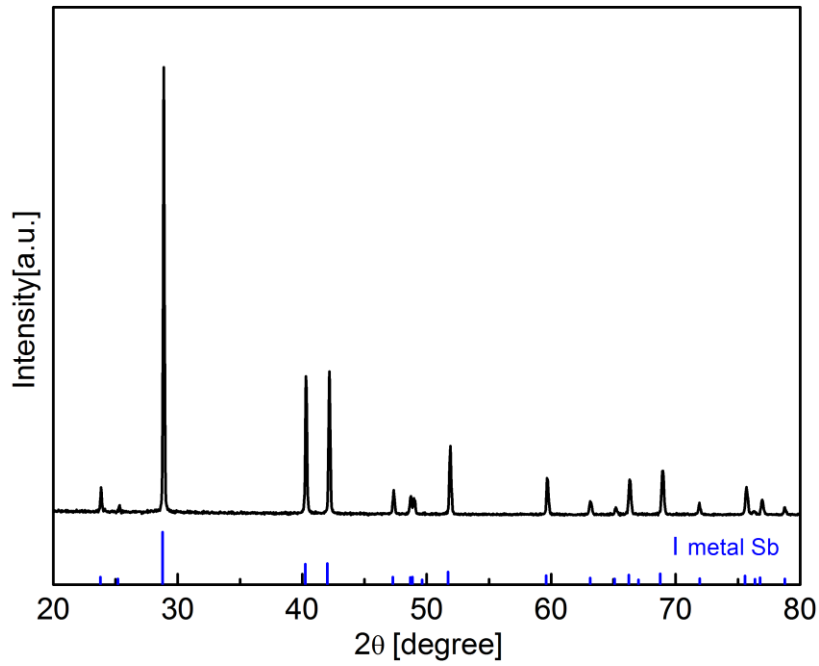

Figure A1. XRD pattern of metallic Sb synthesized under the same condition as those doped In_2O_3 NCs. Bulk reference pattern for metallic Sb is shown in blue lines.

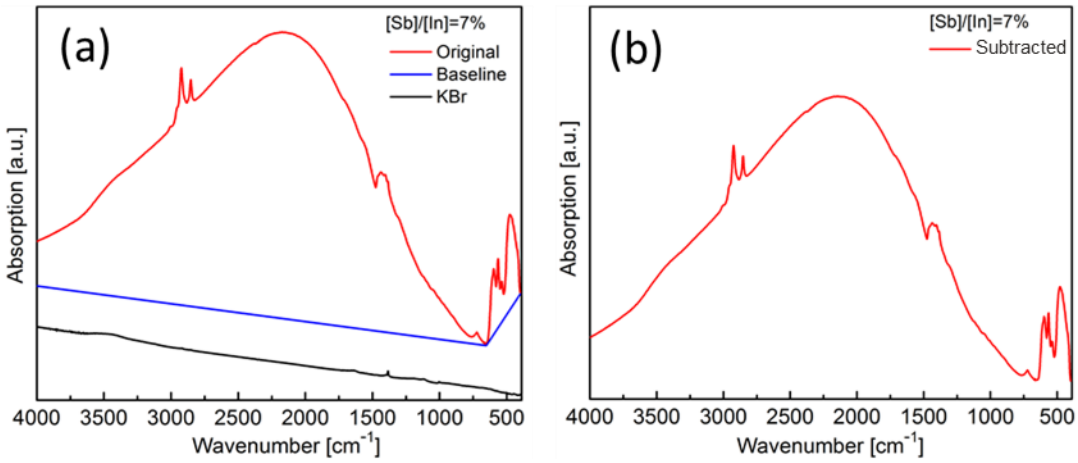

Figure A2. Representive data analysis for 7% AIO NCs before (a) and after (b) background subtraction.

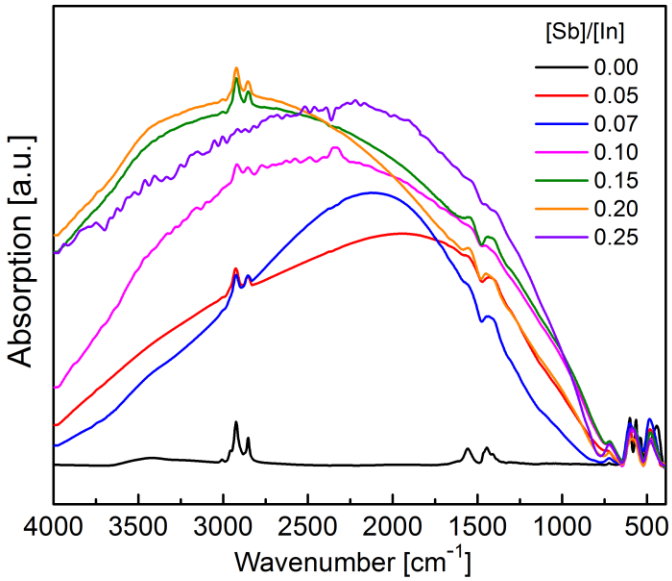

Figure A3. Normalized FTIR spectra of AIO NCs with different precursor concentrations ([Sb]/[In]), as indicated in the graph.

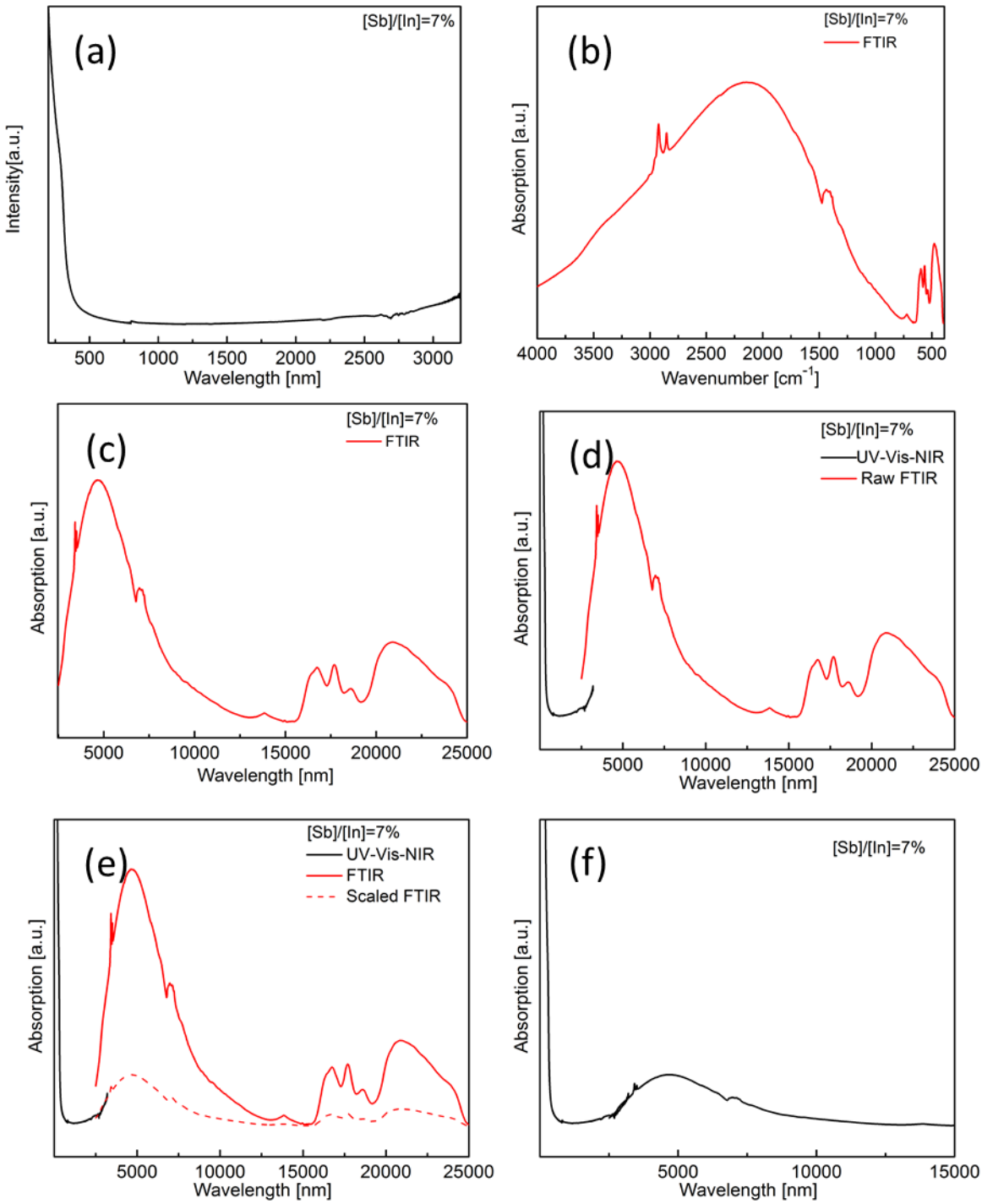

Figure A4. (a) Representative example of a combination of UV-Vis-NIR and FTIR absorption spectra in the case of 7% AIO NCs.

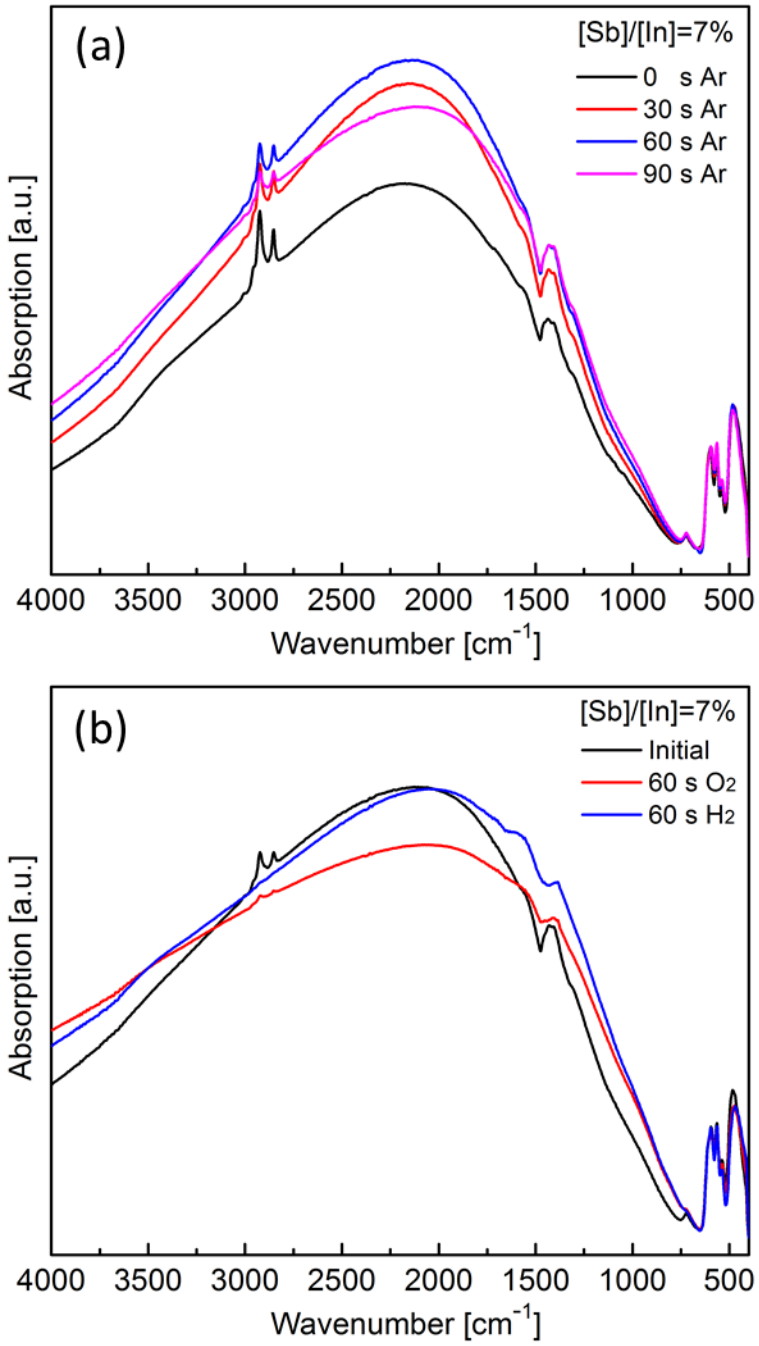

Figure A5. FTIR spectra of 7% AIO NCs annealed under Ar with different duration of time (a) and recovery of FTIR spectra for oxidized 7% AIO NCs by H_2 reduction (b).

Appendix B: Titanium-doped Indium Oxide Nanocrystals

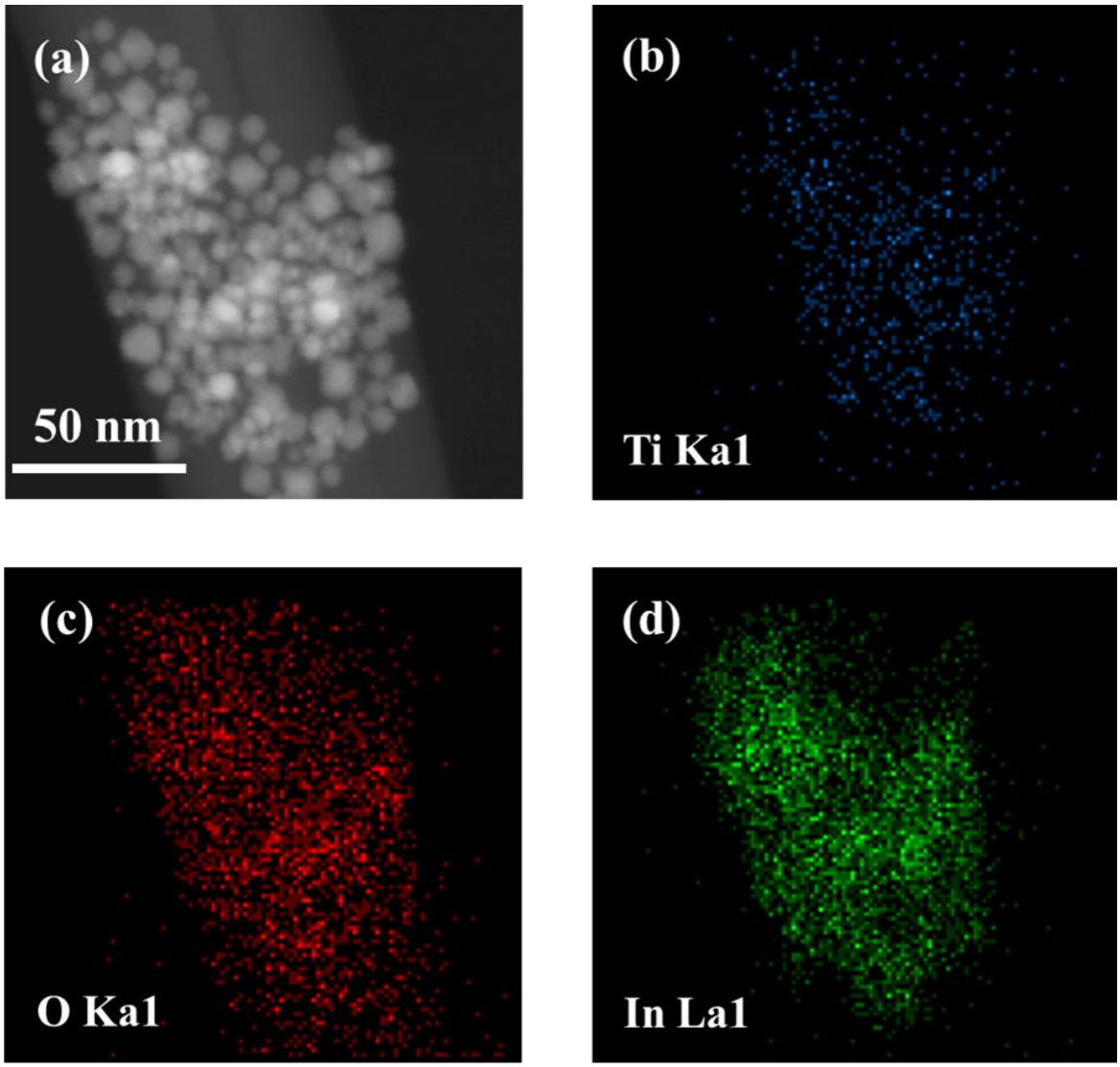

Figure B1: STEM image of the 10% TIO NCs with corresponding EDX elemental maps of Ti, O, and In in STEM.

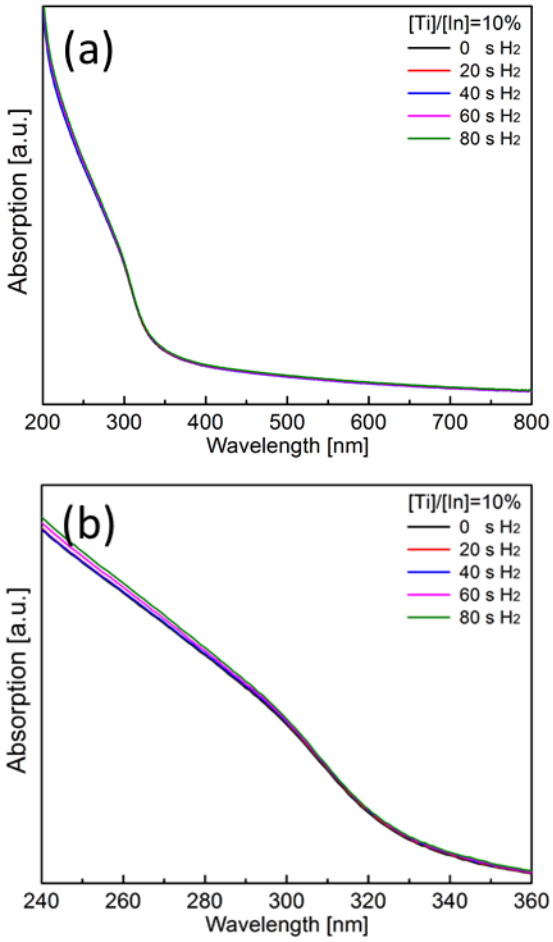

Figure B2: (a) UV-Vis absorption spectra of 10% TIO NCs annealed under H_2 at 400 ^{o}C for various times and (b) enlarged band gap absorption of the spectra.